

Influence of Reconstruction of Arctic Sea Ice Thickness on the Ice-ocean Coupled Forecast in Ice Melting Season

Lu Yang¹, Hongli Fu², Xiaofan Luo¹, Shaoqing Zhang³, and Xuefeng Zhang⁴

¹Tianjin University

²National Marine Data and Information Service

³Physical Oceanography Laboratory, Ocean University of China

⁴School of Marine Science and Technology, Tianjin University

November 21, 2022

Abstract

Generally, the sea ice prediction skills can be improved by assimilating the observed sea ice data into a numerical forecast model to update the initial fields of the model. Meanwhile, it is necessary to assimilate sea ice thickness (SIT) while assimilating sea ice concentration (SIC) to keep the two harmony in assimilation. However, due to the lack of the SIT from satellite remote sensing observation, it cannot meet the bivariate assimilation requirement in Arctic melting season. In order to solve this problem, an easy-to-implement bivariate regression mode of SIT is tentatively established based on the grid reanalysis data of SIC and SIT, through which the SIT field is statistically constructed. Then, the ice-ocean coupled numerical forecast experiment is carried out in which both the observed SIC and the constructed SIT are jointly assimilated using the spatial multi-scale recursive filter (SMRF) method. Results show the joint assimilation of SIC and the constructed SIT can greatly improve the forecast accuracy of sea ice elements especially in the multi-year ice region of Arctic center, where the average absolute error between the SIT forecast and in situ observations is about 0.14 m. Further, effects of the bivariate assimilation on the ocean elements are also deeply investigated in melting season. The higher forecast skill of sea surface temperature and drift flow can be obtained via the bivariate assimilation scheme considering the ice-ocean coupled dynamics and the feedback process between them.

1 **Influence of Reconstruction of Arctic Sea Ice Thickness on the Ice-ocean Coupled**
2 **Forecast in Ice Melting Season**

3 **Lu Yang¹, Hongli Fu², Xiaofan Luo¹, Shaoqing Zhang³, Xuefeng Zhang^{1,*}**

4 ¹School of Marine Science and Technology, Tianjin University, Tianjin, China

5 ²Key Laboratory of Marine Environmental Information Technology, National Marine Data
6 and Information Service, Ministry of Natural Resources, Tianjin, China

7 ³Key Laboratory of Physical Oceanography, Ministry of Education, Ocean University of
8 China, Qingdao, China

9
10 Corresponding author: X. Zhang (xuefeng.zhang@tju.edu.cn)

11 **Key Points:**

- 12 • A bivariate sea ice thickness regression mode provides the possibility for the record of
13 Arctic sea ice thickness in the melting season.
- 14 • The forecast accuracy of sea ice variables can be improved via the joint assimilation of
15 sea ice concentration and reconstructed sea ice thickness.
- 16 • The higher forecast skill of sea surface temperature and drift flow can be obtained
17 through the ice-ocean coupled feedback process.

18 Abstract

19 Generally, the sea ice prediction skills can be improved by assimilating the observed sea
20 ice data into a numerical forecast model to update the initial fields of the model. Meanwhile,
21 it is necessary to assimilate sea ice thickness (SIT) while assimilating sea ice concentration
22 (SIC) to keep the two harmony in assimilation. However, due to the lack of the SIT from
23 satellite remote sensing observation, it cannot meet the bivariate assimilation requirement in
24 Arctic melting season. In order to solve this problem, an easy-to-implement bivariate
25 regression mode of SIT is tentatively established based on the grid reanalysis data of SIC and
26 SIT, through which the SIT field is statistically constructed. Then, the ice-ocean coupled
27 numerical forecast experiment is carried out in which both the observed SIC and the
28 constructed SIT are jointly assimilated using the spatial multi-scale recursive filter (SMRF)
29 method. Results show the joint assimilation of SIC and the constructed SIT can greatly
30 improve the forecast accuracy of sea ice elements especially in the multi-year ice region of
31 Arctic center, where the average absolute error between the SIT forecast and in situ
32 observations is about 0.14 m. Further, effects of the bivariate assimilation on the ocean
33 elements are also deeply investigated in melting season. The higher forecast skill of sea surface
34 temperature and drift flow can be obtained via the bivariate assimilation scheme considering the
35 ice-ocean coupled dynamics and the feedback process between them.

36 Plain Language Summary

37 In order to improve the prediction skills of Arctic sea ice, it is necessary to assimilate the
38 sea ice observation data into the dynamic model to generate a more realistic initial prediction
39 field. However, during the melting season, sea ice thickness (SIT) is difficult to detect
40 directly by using satellite remote sensing since the inversion algorithms fail to work in the
41 saturated surface water vapor from the surface snow melt. In this study, a simple,
42 easy-to-implement bivariate regression model is put forward to construct SIT using the
43 corresponding sea ice concentration (SIC) observation. Benefitting from the joint assimilation
44 of the observed SIC and the constructed SIT, the prediction accuracy of both sea ice variables
45 and ocean variables is greatly improved. The constructed SIT is expected to provide an

46 available dataset for further research on the Arctic sea ice prediction during the melting
47 season.

48 **1 Introduction**

49 The Arctic is one of the most important regions for the exchange of materials and energy
50 between the atmosphere and the ocean, and it plays a significant role in global climate change.
51 The major interaction between the Arctic Ocean and the global climate system is reflected
52 through the sea ice. However, observations in the past 30 years have shown that Arctic sea ice
53 is undergoing rapid changes (Kwok and Cunningham, 2015). From 1979 to 2017, the sea ice
54 extent decreased by 3.24 million square kilometers in September, with a significant decrease
55 in the Arctic sea ice margin from the Beaufort Sea in the west to the Barents Sea in the north
56 (Liu et al., 2019). As the ice shrinks, the ice floes are thinning. Recent satellite data show an
57 average reduction of about 50% in Arctic SIT compared to submarine sea ice observations
58 during 1958-1976 (Kwok and Rothrock, 2009). The above changes in Arctic sea ice have
59 aroused people's attention and posed major opportunity to Arctic maritime activities, such as
60 polar shipping, fishing and oil/gas resources exploration. Meanwhile, the grasp of SIC, SIT
61 and other information is crucial for polar research (Takuya et al., 2018). Therefore, accurate
62 real-time sea ice prediction has become an urgent need (Eicken, 2013). It is well known that
63 Arctic sea ice dynamics models used for short-term forecasting depend heavily on the initial
64 conditions of the model. Therefore, it is necessary to integrate the sea ice observation data
65 into the numerical forecast model using appropriate data assimilation methods to generate a
66 more realistic prediction initial condition and improve the prediction ability of Arctic sea ice
67 (Lisæter et al., 2003).

68 Lindsay and Zhang (2006) used Nudging method to assimilate SIC observation. The
69 assimilated SIC improves the match with the observed extent, but the sea ice draft in the
70 Fram Strait is underestimated by 0.64m compared with the observation. Lisæter et al. (2003)
71 assimilated SIC observation data using the Ensemble Kalman Filter (EnKF) (Evensen, 1994)
72 based on the coupled ice-sea model. Although the correlation coefficient between the forecast
73 SIC and SIT reaches more than 0.5 in winter, it drops below 0.3 or even reaches a negative

74 value in the melting season. Wang et al. (2013) proposed a method combining optimal
75 interpolation with the Nudging to assimilate SIC. Results show that there are significant
76 improvements for SIC analysis result in the sea ice margin region in summer, but there are
77 deviations in the prediction of sea ice extent. Yang et al. (2015a) used Local Singular
78 Evolution Interpolation Kalman Filter (LSEIK) to assimilate SIC in summer. The consistency
79 of forecast SIC with satellite observations is improved, but the multi-year ice thickness in the
80 central Arctic is overestimated by more than 1m. Previous studies have shown that while the
81 assimilation of observed SIC can improve the SIC forecast results, SIT improvements are
82 insignificant.

83 The study of Day et al. (2014) showed that accuracy of initial SIT is also important for
84 the prediction of SIC and sea ice extent in summer. Lisæter et al. (2007) used EnKF to
85 assimilate the SIT detected by Cryosat satellite and improved the quality of initial SIT. The
86 results showed that the prediction results of SIC, sea surface temperature (SST) and sea
87 surface salinity are improved by the SIT assimilation. Yang et al. (2014) used LSEIK to
88 simultaneously assimilate Special Sensor Microwave Imager/Sounder (SSMIS) SIC and Soil
89 Moisture and Ocean Salinity (SMOS) SIT in the cold season. Compared with only SIC
90 assimilation or no data assimilation, the root mean square error (RMSE) of SIT forecast
91 results is reduced 0.47m. However, SMOS SIT observation data are only applicable to thin
92 ice (<1m) (Tian-Kunze et al., 2014), the assimilation of which only improves the one-year ice
93 prediction in the marginal area of sea ice, while the thick (multi-year) ice cannot be
94 significantly improved during the early melting and freezing seasons (Yang et al., 2016; Xie
95 et al., 2016). In this case, in cold season, Mu et al. (2018b) not only assimilated SMOS SIT
96 and SSMIS SIC observation data, but also simultaneously assimilated Cryosat-2 SIT
97 observation data which can better capture interannual changes of thick ice areas (Laxon et al.,
98 2013). By using the complementary characteristics of the two kinds of thickness data, the
99 overall RMSE of SIT and SIC is smaller than the counterpart under the condition of
100 assimilating both SMOS SIT and SSMIS SIC data.

101 It is worth noting that there are few studies on the prediction of SIT during the melting

102 season due to the sparse in situ observations of SIT. Additionally, the Arctic SIT obtained
103 from satellite remote sensing inversion has only been available in the recent decade with the
104 time coverage ranging from October to April (Ricker et al., 2014; Ricker et al., 2017),
105 resulting in insufficient SIT observations during the melting season. In order to solve this
106 problem, Mu et al. (2018a) combined the skill of satellite thickness assimilation in the
107 freezing season with the model skill in the melting season, and a combined model and
108 satellite thickness (CMST) is proposed to estimate the thickness of Arctic sea ice in the
109 melting season. Yang et al. (2019) used the Nudging method to assimilate the CMST
110 estimated SIT in the cold season to provide the initial state of the model for the melting
111 season, so that the SIT in summer can be modified by the positive cross relationship between
112 SIC and SIT. In addition, an integrated sea ice seasonal prediction system (SISPS) is designed
113 for the real-time prediction of summer sea ice conditions in the Arctic. CMST estimation is
114 heavily dependent on the quality of satellite data products and the parameterization of
115 physical processes in the model, which has certain uncertainties (Mu et al., 2018a).

116 This paper proposed a bivariate regression model of SIT based on the fact that there is a
117 strong positive correlation between SIC and SIT from the perspective of statistical
118 significance (Yang et al., 2015b), so that the "pseudo" observation field of SIT can be
119 constructed by using satellite remote sensing observation data of SIC. On this basis, the
120 SMRF data assimilation method is used to assimilate the sea ice multi-element data to
121 improve the initial field of the model. The traditional data assimilation methods used by other
122 scholars (such as LSEIK, Nudging, 3DVAR, etc.) face with the problems that the
123 determination of correlation scale and filtering parameters depends on human experience and
124 the non-objectivity of the background error covariance estimation cannot be effectively
125 solved (Wu et al., 2015). In contrast, the SMRF data assimilation method can not only correct
126 the error of long wavelength information in the whole region, but also modify the error of
127 short wavelength information in the data intensive region, so that the multi-scale information
128 decomposed from the observation can be once extracted successively from the long
129 wavelength to the short wavelength (Zhang et al., 2020).

130 The paper is organized as follows: the ice-ocean coupled model is presented in Section 2
131 and the data sources including sea ice and ocean are described in Section 3. In Section 4, two
132 core methods of the bivariate SIT regression mode and the SMRF data assimilation method
133 are introduced. The accuracy of the SIT field constructed by the regression model is tested
134 based on an idealized twin experiment framework in Section 5. On this basis, in Section 6,
135 the influence of multi-scale joint assimilation of SIC and SIT on the prediction results of sea
136 ice and ocean elements is explored based on the ice-ocean coupled model, and the interaction
137 between the predicted SIC and SIT is discussed. Finally, the conclusion and summary of this
138 study are in Section 7.

139 **2 The ice-ocean coupled model**

140 The ocean model used is the Massachusetts Institute of Technology General Circulation
141 Model (MITgcm) (Marshall et al., 1997), which solves the three-dimensional primitive
142 equations with implicit linear free-surface under the hydrostatic and Boussinesq
143 approximations. The ocean model is coupled to a sea-ice model that computes ice thickness,
144 ice concentration, and snow cover as Zhang et al. (1998) and that simulates a viscous-plastic
145 rheology using an efficient parallel implementation of the Zhang and Hibler (1997) solver.
146 The coupled model used in this study adopts a global cubic spherical grid, and the Arctic
147 region includes 510×510 grid points with an average horizontal distance of 18 km. The open
148 boundary is about 55°N in the Atlantic Ocean and Pacific Ocean.

149 The atmospheric forcing fields include 10m surface wind speed, 2m temperature,
150 relative humidity, precipitation, downward longwave and shortwave radiations. Through the
151 two-way coupled between ice and sea, the ocean model provides the sea ice model with
152 information such as ablation/freezing potential, SST and salinity, surface velocity, while the
153 sea ice model provides the information of the SIC, fresh water and salinity fluxes, ice-sea
154 stress and others. The heat flux on the sea ice surface is referred to the results of Parkinson
155 and Washington (1979). The change of sub-grid ice thickness in the sea ice model is taken
156 into account in the calculation of conduction heat flux. In other words, the sea ice is divided
157 into 7 categories according to the SIT value in a horizontal grid. The variation of heat flux

158 and albedo caused by snow cover and the process of snow-ice conversion are considered on
159 the surface of sea ice. The albedo of dry ice, wet ice, dry snow and wet snow is 0.87, 0.78,
160 0.98 and 0.80, the sea-ice drag coefficient is 5.2, and the sea-ice intensity is $2.7 \times 10^4 \text{Pa}$
161 (Losch et al., 2010).

162 **3 Data sources**

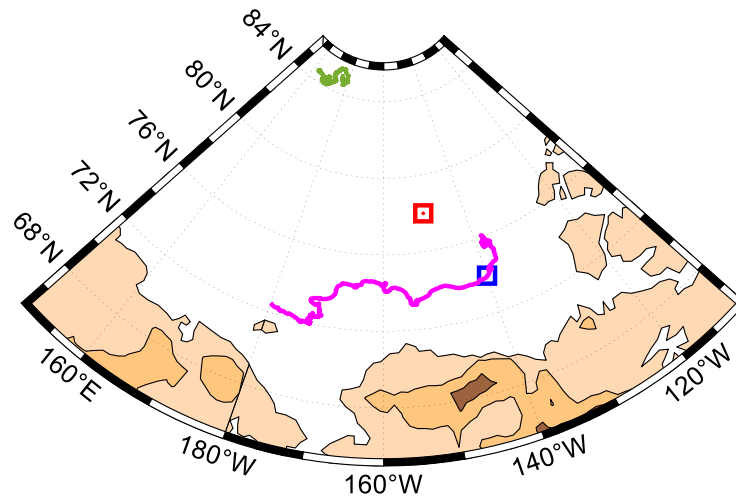
163 Observations of satellite remotely sensed SIC, independent ice thickness data and SST
164 data are utilized.

165 SIC refers to the proportion of sea ice covered area in unit space, the variation range of
166 which is 0-1. The observations of daily SIC are derived from the daily passive microwave
167 data of the special sensor microwave imager (SSM/I) carried by DMSP F-17. It was
168 processed by National Snow and Ice Data Center (NSIDC) with NASA team algorithm
169 (Cavalieri et al., 2012). The spatial resolution is $25 \text{ km} \times 25 \text{ km}$.

170 To assess our predicted SIT results, independent in situ SIT data are used. One is sea ice
171 draft, which comes from Upward Looking Sonar (ULS) measurements of Beaufort Gyre
172 Experiment Program (BGEP). It can be converted into thickness by multiplying by 1.1, which
173 is approximately equal to the ratio of mean seawater density of 1024 kg/m^3 and sea ice
174 density of 910 kg/m^3 (Nguyen et al., 2011). The error of ULS measurements of ice draft is
175 estimated about 0.1m (Melling et al., 1995). The other is SIT data, which is derived from Ice
176 Mass balance Buoys (IMB) deployed on the surface of Arctic sea ice (Perovich et al., 2009).
177 The two acoustic rangefinders on the IMB monitor the position of the ice bottom and the
178 snow and ice surface, which is used to estimate the SIT. The accuracy of both detectors is 5
179 mm (Richter-Menge et al., 2006). According to needs for the research, the data from mooring
180 facilities of the BGEP_2011B located in ($78^\circ 0.395' \text{ N}$, $149^\circ 58.462' \text{ W}$), BGEP_2011D
181 located in ($73^\circ 59.649' \text{ N}$, $139^\circ 59.043' \text{ W}$) and ice mass balance drift buoys of the
182 IMB_2011K in the Beaufort Sea during 1 September to 7 October 2011 are selected. In
183 addition, ice mass balance drift buoys of the IMB_2011L in the North Pole Center during 13
184 September to 7 October 2011 is also selected. The position of mooring facilities and buoy

185 drift trajectory are shown in Figure 1.

186



187

188 **Figure 1.** The location of mooring facilities BGEF_2011B (red box) and BGEF_2011D (blue box) and the
 189 drift track of buoys IMB_2011K (pink line) and IMB_2011L (green line).

190

191 Daily observations of SST are from the European Space Agency (ESA) Climate Change
 192 Initiative's Sea Surface Temperature Project. The dataset is named SST_cci OSTIA Level 4
 193 Analysis Climate Data Record, version 2.1. It combines data from the Advanced Very
 194 High-Resolution Radiometer (AVHRR) and the Along Track Scanning Radiometer (ATSR).
 195 Data assimilation method is used to provide SST fusion data with a spatial resolution of
 196 $0.05^\circ \times 0.05^\circ$ (Merchant et al., 2019).

197 The reanalysis data are from TOPAZ4 version of the Nansen Centre for Environment
 198 and Remote Sensing, Norway's Sea Ice/Ocean Numerical Prediction System (Xie et al., 2017).
 199 The dataset is named Arctic_Reanalysis_Phys_002_003. It includes daily SIC, SIT and sea
 200 ice velocity. The spatial resolution is $12.5\text{km} \times 12.5\text{km}$, the time range is from January 1, 1991
 201 to December 31, 2019, and the region covers the Arctic Ocean.

202 4 Method

203 4.1 Bivariate SIT regression mode

204 Considering that it is impossible to obtain Arctic SIT observation from the satellites

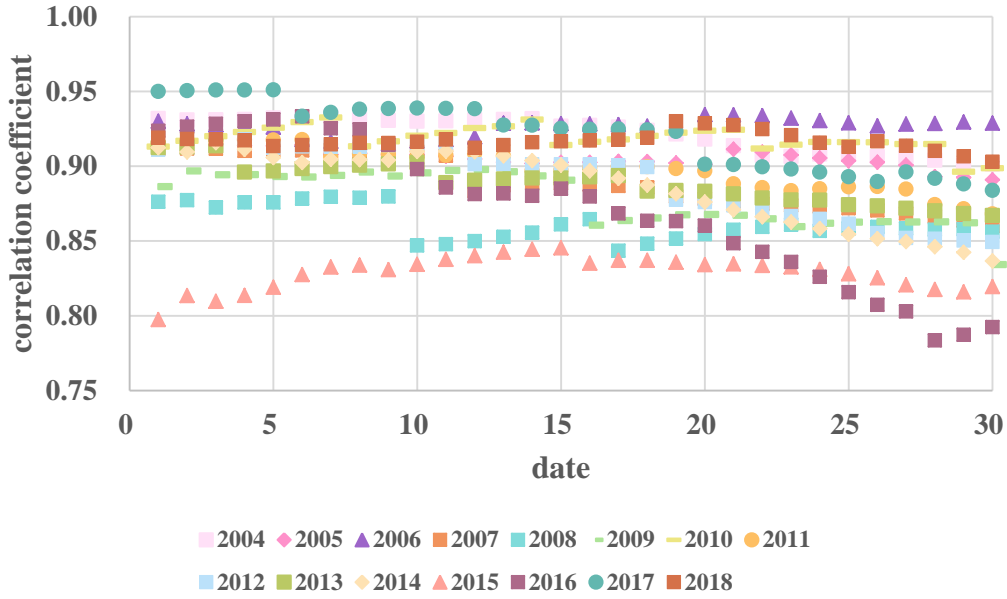
205 remote sensing in the melting season due to that the most advanced inversion algorithm was
 206 impeded by the saturated surface water vapor from the surface snow melt (Ricker et al.,
 207 2017), we focus on the reconstruction of SIT in the melting season (i.e., September).
 208 Meanwhile, because the smallest SIT was recorded in the past 40 years (Min et al., 2019), the
 209 autumn of 2011 (from 1 September to 30 September 2011) is chosen as an example to
 210 develop the bivariate regression mode for SIT.

211 First of all, in order to construct SIT field from 1 September to 30 September 2011, the
 212 TOPAZ4 reanalysis SIC and SIT data of the first 7 years (2004-2010) and the last 7 years
 213 (2012-2018) are selected. In order to verify the validity of the dataset, the spatial correlation
 214 coefficients between SIC and SIT on each day in September of each year are calculated
 215 respectively, and the calculation formula is shown in Eq. (1). According to the scatter plots
 216 between correlation coefficients and dates (Figure 2), except for a few dates, most of the
 217 correlation coefficients between SIC and SIT are between 0.80 and 0.95, which completely
 218 pass the significance test. It indicates that there is a strong correlation between SIC and SIT,
 219 which provides theoretical support for the establishment of regression mode in the next step.

$$220 \quad coef = \frac{\sum_{i=1}^n (x_i - \bar{x})(y_i - \bar{y})}{\sqrt{\sum_{i=1}^n (x_i - \bar{x})^2 \sum_{i=1}^n (y_i - \bar{y})^2}} \quad (1)$$

221 Where, i represents the label of grid point, x_i represents the value of SIC of the i -th grid
 222 point, y_i represents the value of SIT of the i -th grid point, \bar{x} represents the average value
 223 of SIC at all grids, and \bar{y} represents the average value of SIT at all grids.

224



225

226 **Figure 2.** Spatial correlation coefficient between daily SIC and SIT in September from 2004 to 2018.

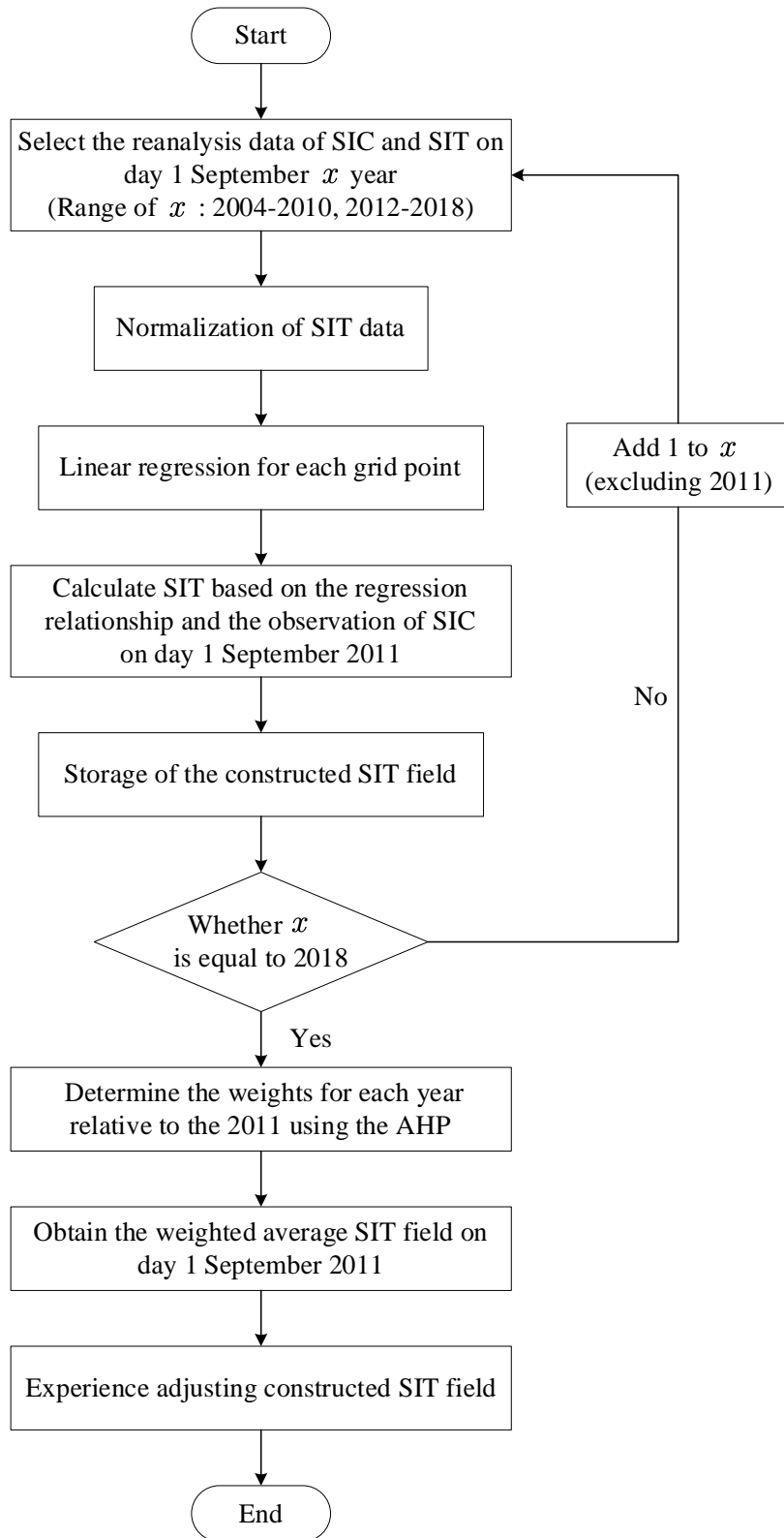
227

228 The following is an example of 1 September 2011 to illustrate the construction process
 229 of SIT. The flow chart is shown in Figure 3. First of all, the reanalysis data of daily SIC and
 230 SIT on 1 September in 14 years from 2004 to 2010 and from 2012 to 2018 are selected. In
 231 order to prevent "overfitting" in the calculation process, the SIT data are normalized and
 232 converted into a scalar quantity, which is limited in the interval of [0, 1], as follows:

$$233 \quad x'_k = \frac{x_k - x_{\min}}{x_{\max} - x_{\min}} \quad (2)$$

234 where, x_k is original data at the k -th grid point in each year, x'_k is the result of
 235 normalization of x_k , x_{\min} is the minimum value of SIT at all grids in each year, x_{\max} is
 236 the maximum value of SIT at all grids in each year.

237



238

239 **Figure 3.** A flow chart of bivariate SIT regression model (take 1 September 2011 as an example).

240

241

242 Then, the linear regression with SIC as independent variable and SIT as dependent
 243 variable is made at each grid point of the whole region for each year based on the reanalysis
 244 data of daily SIC and SIT. The corresponding SIC-SIT regression relation at each grid can be
 245 obtained for each year. The formula is as follows:

$$246 \quad y = ax \quad (3)$$

247 where, a is the undetermined coefficient, x is the value of SIC, and y is the value of SIT
 248 corresponding to x .

249 The 14 sets of SIT fields on 1 September 2011 are calculated from the fitting relation
 250 and the SIC observational data. The 9-quartile scale method in the Analytic Hierarchy
 251 Process (AHP) (Rahman & Frair, 1984) is used to determine the weight of each year relative
 252 to 2011, as shown in Table 1 (all results pass the consistency test). The constructed SIT field
 253 on 1 September 2011 is obtained by weighting average.

254 Finally, according to the SIC observational data, the SIT field is empirically adjusted to
 255 make the constructed SIT consistent with the SIC (Preller et al., 2002): if the value of SIC at
 256 a certain grid point is 0 and the constructed SIT at this grid point is not 0, the ice will be
 257 removed from the constructed SIT field; If the value of constructed SIT at a certain grid point
 258 is 0 and the SIC at this grid point is not 0, the constructed SIT is adjusted to 1.0m (if SIC >
 259 0.5) or 0.5m (if SIC < 0.5). The adjusted SIT field can be treated as the SIT observation field
 260 of 1 September 2011 in the process of data assimilation.

261

262 **Table 1.** *The weights for years in 2004-2010 and 2012-2018 relative to year 2011*

	2004	2005	2006	2007	2008	2009	2010
Weight	0.0156	0.0224	0.0338	0.0518	0.0793	0.1200	0.1771
	2012	2013	2014	2015	2016	2017	2018
Weight	0.1771	0.1200	0.0793	0.0518	0.0338	0.0224	0.0156

263

264 4.2 The SMRF data assimilation method

265 The traditional three-dimensional variational (3DVAR) data assimilation methods can
266 only correct the error of a certain wavelength in the assimilation process. Xie (2005) shows
267 that in the process of data assimilation, if the error of long wavelength could not be well
268 corrected, the short wavelength error could not be well corrected either. The SMRF is a
269 method that can realize the sequential correction from long wavelength to short wavelength
270 and extract multi-scale information through a single 3DVAR analysis (Zhang et al., 2020).

271 In this method, firstly, a recursive filter operator \mathbf{B} with the small filter parameter β
272 is applied to the initial guess field. The parameter β is set to small value in order to ensure
273 that information of all scales could pass. The cost function and its gradient are calculated
274 based on the filtered initial guess field. Then, another recursive filter operator \mathbf{E} with the
275 parameter α is applied to the negative gradient of the cost function. This filter parameter α
276 should select a larger value at the beginning to extract the "longest" wavelength information
277 in the observational data. A line search process (More and Thuente 1992) is performed along
278 this gradient direction to find the appropriate step size, and the estimated value is updated.
279 The observational residual is obtained by removing the extracted signal from the observation
280 data. Then, the filter parameter α is appropriately reduced to extract the "maximum" scale
281 signal in the observational residual at current iteration. As the number of iterations increases,
282 the filter parameter α sequentially decreases, so that the information of each scale can be
283 extracted successively from long wavelength to short wavelength in order to obtain the
284 analyzed field.

285 Compared with traditional data assimilation methods, SMRF not only possesses a good
286 ability in propagating observational signals, but also shows a superior performance in
287 extracting multi-scale information resolved in observation by performing 3DVAR once
288 (Zhang et al., 2020). Based on the above two points, the SMRF is applied to assimilate the
289 observed SIC and constructed SIT into initial fields for sea ice prediction experiments.

290 **5 The twin test**

291 5.1 Experiment design

292 In order to evaluate the SIT constructed by the bivariate SIT regression mode and its
 293 influence on the ice-sea coupled prediction, four prediction experiments are designed within
 294 an idealized twin experiment framework. The initial SIC and the SIT fields from four Exps
 295 are given in Table 2. The ice-ocean coupled MITgcm model is used to perform 120h
 296 prediction.

297

298 **Table 2.** *Comparison of the initial fields of twin experiments*

	Sea ice concentration	Sea ice thickness
Control Exp	The model result on 1 Sep 2011	The model result on 1 Sep 2011
Exp 1	The model result on 1 Sep 2012	The model result on 1 Sep 2012
Exp 2	Same as Exp 1, but the SIC initial field in control Exp is assimilated	Empirically adjusted the SIT initial field in Exp 1
Exp 3	Same as Exp 2	Same as Exp 1, but the constructed SIT is assimilated

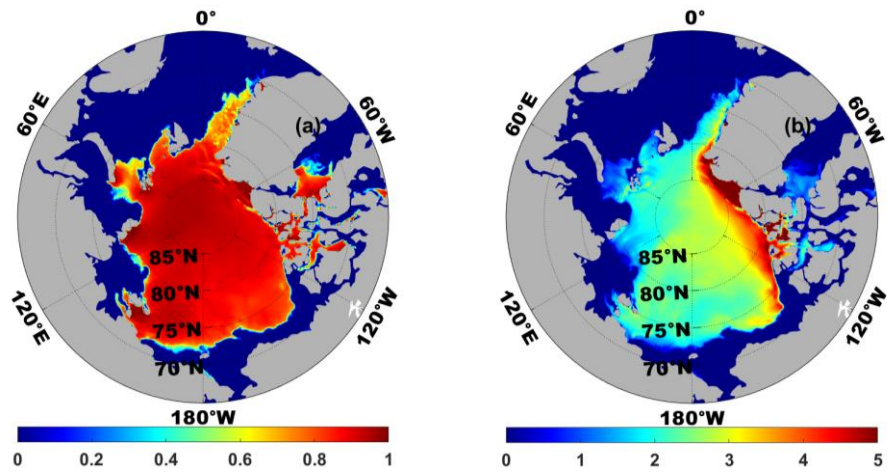
299

300 In control Exp, the SIC and SIT initial fields (Figure 4) are the simulation results of the
 301 ice-sea coupled model on 1 September 2011, which is used as the "truth" field for the
 302 comparison of Exp 1-3. The prediction results of control Exp also serve as the "truth" field
 303 without deviation.

304 In Exp 1, all configurations are the same as the control Exp except employing the model
 305 results of SIC and SIT on 1 September next year (Figure 5) as a "biased" initial field of this
 306 year. In control Exp and Exp 1, the model results of different years are used as the initial
 307 fields, which not only makes the "truth" and the "biased" fields have obvious difference, but
 308 also ensures that the SIC matches with the SIT.

309

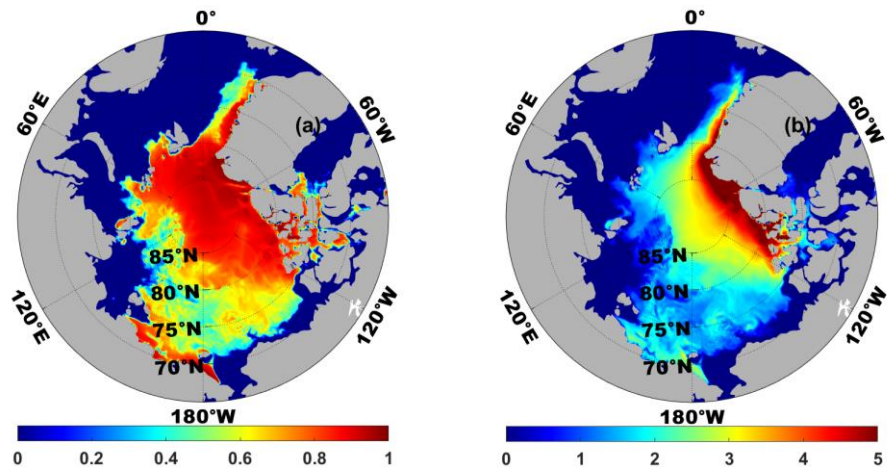
310



311

312 **Figure 4.** The SIC (a) and the SIT (b, unit: m) on 1 September 2011 for initial fields in control Exp.

313



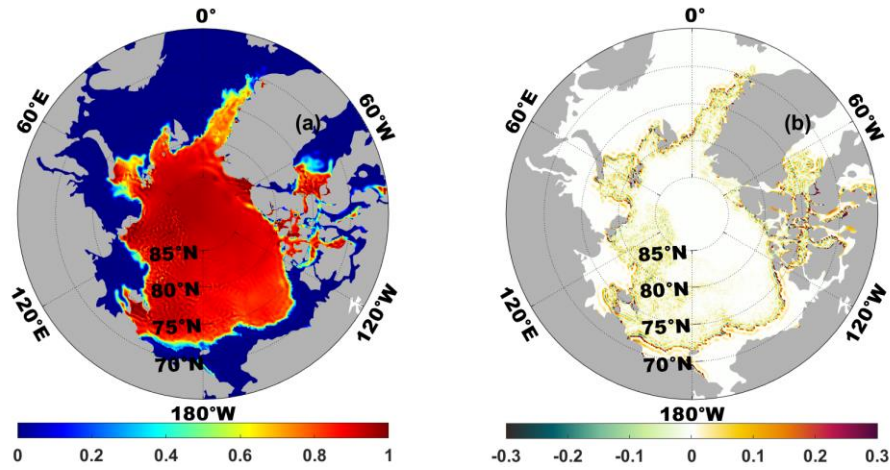
314

315 **Figure 5.** The SIC (a) and the SIT (b, unit: m) fields on 1 September 2012 for initial fields in Exp 1.

316

317 In Exp 2, all configurations are the same as the Exp 1 except that the initial SIC (Figure
 318 6a) is changed to the analyzed result derived from assimilating the SIC "observations"
 319 (Figure 4a) and the initial SIT (Figure 7a) is empirically adjusted according to the SIC change
 320 in order to keep the physical consistency between SIC and SIT.

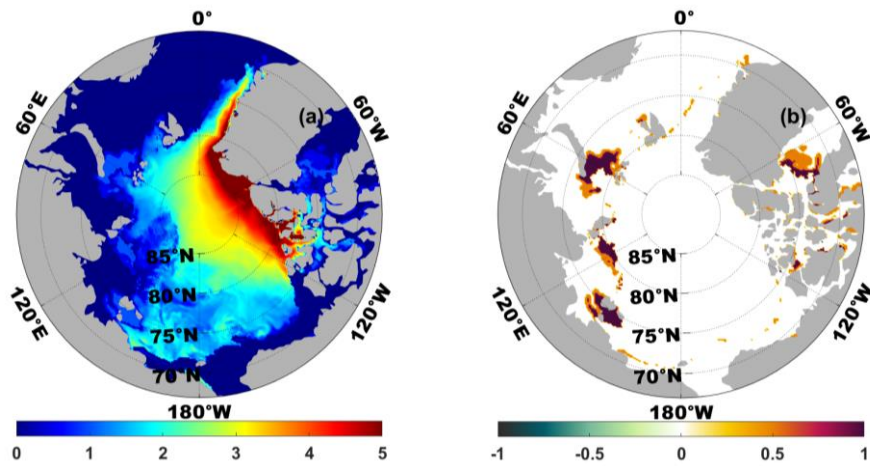
321



322

323 **Figure 6.** (a) The SIC initial field in Exp 2; (b) The difference between the SIC initial field in Exp 2 and
 324 the SIC initial field in control Exp.

325



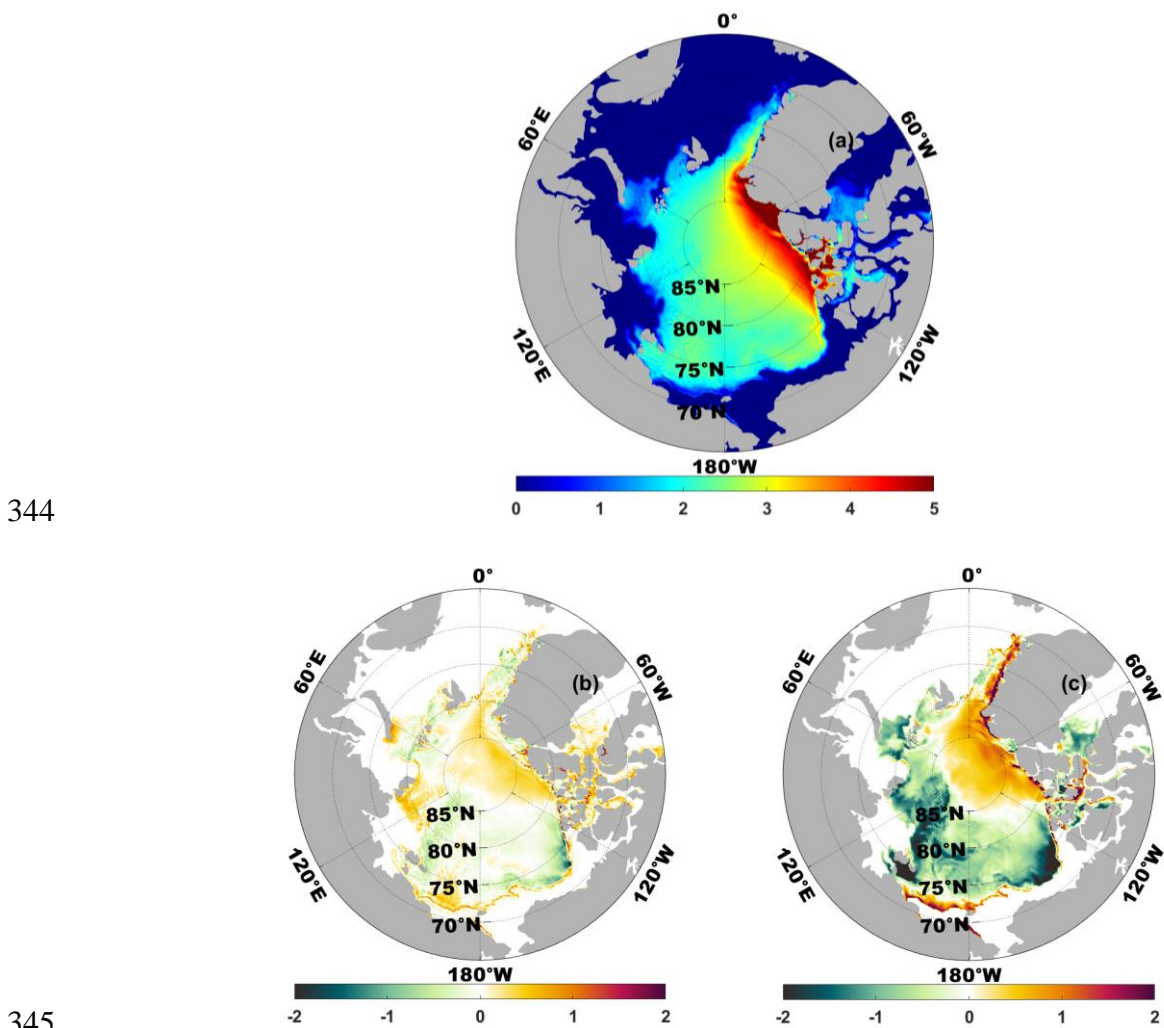
326

327 **Figure 7.** (a) The SIT initial field in Exp 2 (unit: m); (b) The difference between the SIT initial field in Exp
 328 2 and the SIT initial field in Exp 1 (unit: m).

329

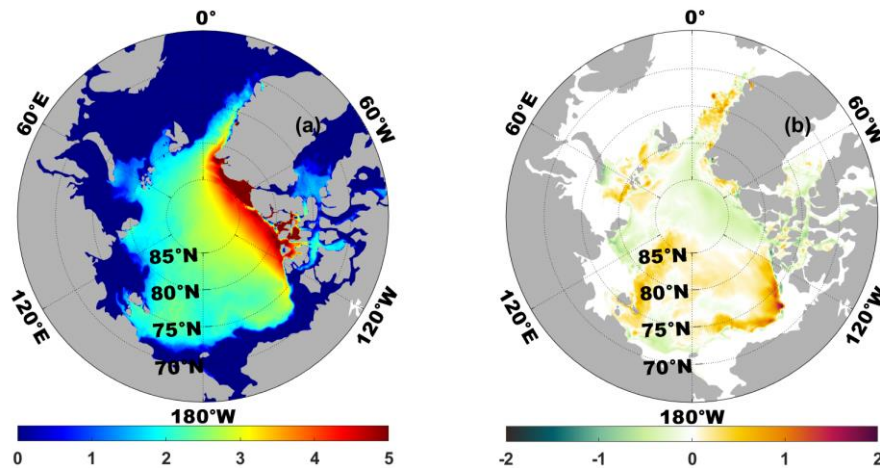
330 In Exp 3, all configurations are the same as the Exp 2 except that the initial SIT (Figure
 331 8a) is changed to the analyzed result derived from assimilating the constructed SIT (Figure
 332 9a). The constructed SIT is obtained by using the bivariate SIT regression mode. The
 333 construction process is the same as shown in Figure 3, which only needs to replace the
 334 reanalysis data with the simulation results and replace the observed SIC with the initial SIC
 335 of control Exp.

336 The difference between the constructed SIT and the SIT initial field in control Exp is
 337 shown in Figure 9b. The RMSE of the two is 0.0877. It is much smaller than the average SIT
 338 of the initial field in control Exp, which is 2.33 m. In addition, the RMSE between the initial
 339 field in Exp 3 and the SIT initial field in control Exp is 0.1482 (Figure 8b), which is
 340 extremely smaller than that between the initial field in Exp 2 and the initial field in control
 341 Exp (0.2764, Figure 8c). It can be seen that the assimilation of the constructed SIT can
 342 effectively improve the accuracy of the initial field and make it closer to the "truth" field.
 343



346 **Figure 8.** (a) The SIT initial field in Exp 3 (unit: m); (b) The difference between the initial field in Exp 3
 347 and the SIT initial field in control Exp (unit: m); (c) The difference between the SIT initial field in Exp 1
 348 and the SIT initial field in control Exp (unit: m).

349



350

351 **Figure 9.** (a) The constructed SIT in Exp3 (unit: m); (b) The difference between the constructed SIT and
 352 the SIT initial field in control Exp (unit: m).

353 5.2 Results

354 To further evaluate whether the assimilation of the constructed SIT has a positive effect
 355 on the prediction of ocean and sea ice, the prediction accuracy of SIC, SIT, SST and sea ice
 356 drift are analyzed.

357 The RMSEs of the forecast SIC, SIT and SST in Exp 1, Exp 2, Exp 3 relative to that in
 358 control Exp are shown in Table 3. It is not difficult to see that the RMSEs of SIC in Exp 2
 359 and Exp 3 are much smaller than that in Exp 1, which indicates that the assimilation of SIC in
 360 the initial field plays a vital role in improving the SIC prediction accuracy. It is particularly
 361 noted that although the same initial field of SIC is used in Exps 2 and 3, the RMSE of SIC in
 362 Exp 3 is smaller than that in Exp 2. So, the joint assimilation of the SIC and the constructed
 363 SIT in Exp 3 makes the initial SIC and SIT match better physically, which indirectly
 364 improves the prediction accuracy of SIC. The RMSE of the SIT in Exp 3 is far less than those
 365 in Exps 1 and 2, which also implies that the SIT field constructed by the bivariate SIT
 366 regression mode is more effective and accurate.

367

368

369

370

371

Table 3. *The RMSEs of SIC, SIT and SST in Exps 1 - 3 during the prediction time of 24-120h*

Variable	Exps	Prediction time				
		24h	48h	72h	96h	120h
SIC	Exp 1	0.1118	0.1123	0.1124	0.1124	0.1126
	Exp 2	0.0247	0.0297	0.0348	0.0395	0.0418
	Exp 3	0.0234	0.0288	0.0340	0.0379	0.0391
SIT	Exp 1	0.3007	0.3017	0.3025	0.3035	0.3058
	Exp 2	0.2609	0.2617	0.2655	0.2686	0.2706
	Exp 3	0.1070	0.1128	0.1184	0.1227	0.1240
SST	Exp 1	0.8109	0.8140	0.8183	0.8193	0.8250
	Exp 2	0.7704	0.7709	0.7820	0.7890	0.8118
	Exp 3	0.7684	0.7690	0.7805	0.7886	0.8114

372

373

374

375

376

377

378

379

380

381

382

383

384

385

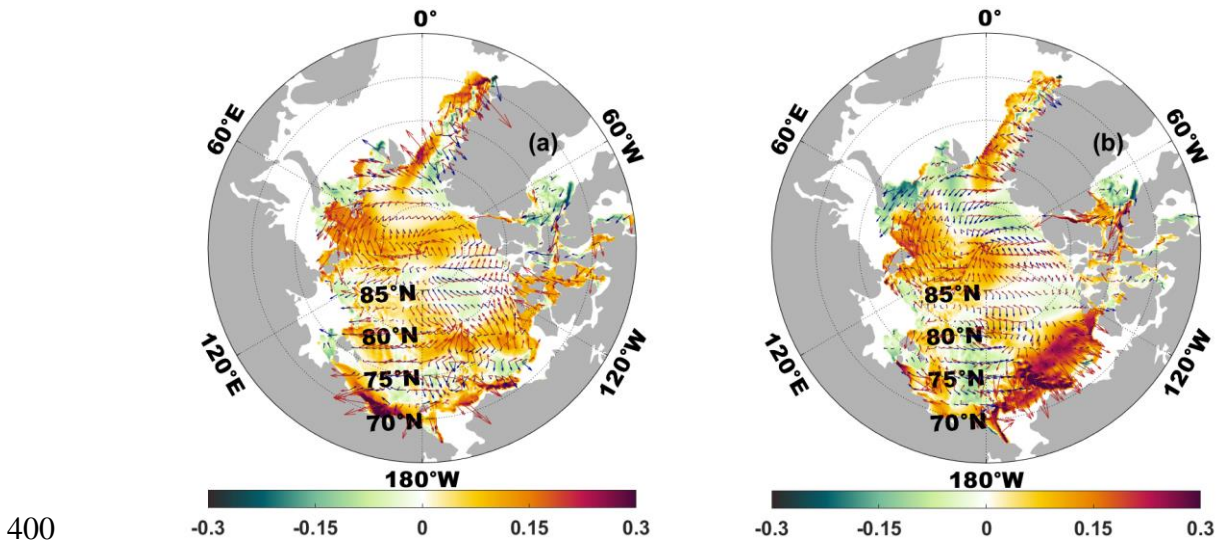
386

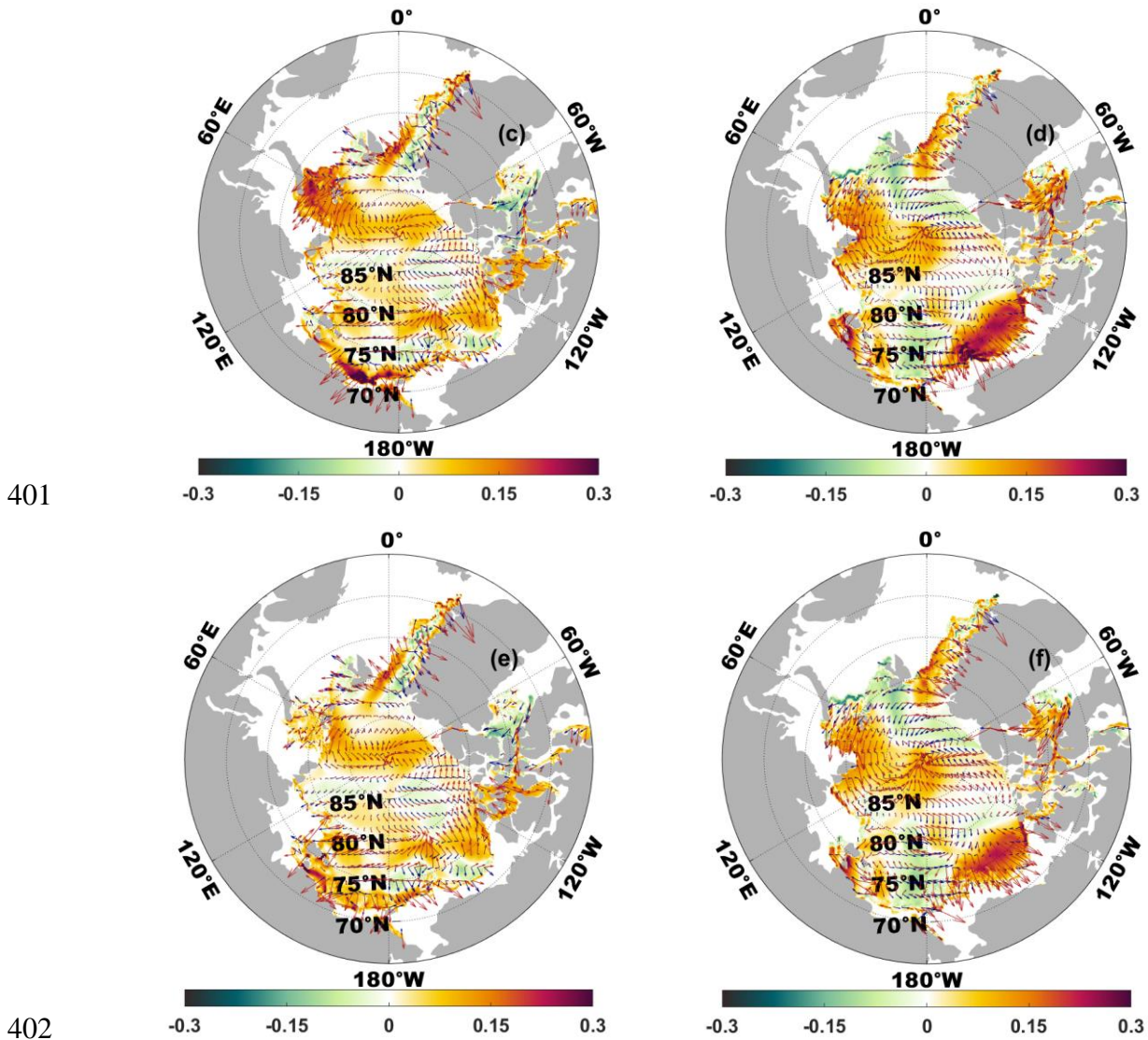
Sea ice is closely related to SST. High SST can release heat to sea ice, resulting in sea ice fusion. Low SST can absorb heat from sea ice and increase the thickness or area of sea ice. Therefore, although SST is not assimilated in the three experiments, their prediction accuracy is related to the initial SIC and SIT accuracy. Although the RMSEs of SST prediction results in the three experiments are not significantly different, the relationship of the SST RMSEs in three experiments is as follows: Exp 3 < Exp 2 < Exp 1 (Table 3). The RMSEs in Exp 3 are minimum in the whole prediction time. The SST short-term forecast results (24h and 48h) in Exp 3 are obviously better than those of the other two experiments. So, the higher the accuracy of initial SIC and SIT, the lower the error of SST prediction.

Sea ice divergence can reduce the local SIT and SIC; on the contrary, sea ice convergence can increase the SIT and SIC. At the same time, the thick ice is not easy to be accelerated by the wind and ocean current under the influence of the strong internal stress; on the contrary, the thin ice is easy to be accelerated due to the weakening of internal stress. So, sea ice velocity is also closed to the SIT and SIC. When the SIT and SIC are assimilated in

387 the initial field, the accuracy of sea ice velocity is also affected. Just as shown in Figure 10a,
 388 c and e, it is not difficult to see that the forecast results of 24h sea ice velocity direction in
 389 Exps 1 and 2 are apparently different from the "true" field. In addition, compared with the
 390 "true" field, the sea ice velocity of Exp 1 and 2 differ greatly in the Kara Sea, the Chukchi
 391 Sea and the East Siberian Sea. This may be due to the lower initial ice thickness value in
 392 these regions than the "true" field. Under the same atmospheric and ocean current driving
 393 conditions, the thin ice is easy to be accelerated. Although the results of Exp 3 are different
 394 from those of the "true" field, the drift direction and velocity in the Barents Sea and the East
 395 Siberian Sea are closer to those of the "true" field relative to the other two experiments. The
 396 RMSE of sea ice velocity in Exp 3 is 22.4% lower than that in Exp 1, and 16.9% lower than
 397 that in Exp 2. A similar conclusion can be drawn from the 120h forecast results (Figure 10b, d
 398 and f).

399





403 **Figure 10.** Difference of the sea ice velocity (color map) between the "true" field and the forecast results
 404 for Exp 1 (a, b), Exp 2 (c, d) and Exp 3 (e, f) at 24h (a, c, e) and 120h (b, d, f). And comparison of the sea
 405 ice drift (arrows) between the "true" field (blue) and the forecast results (red) for Exp 1, Exp 2 and Exp 3 at
 406 24h and 120h (unit: m/s).

407 **6 Retroactive real-time forecast experiments**

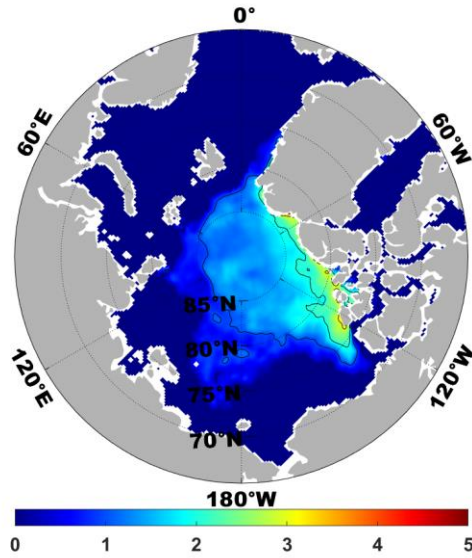
408 In order to further explore the validity of the SIT field constructed by the bivariate
 409 regression mode under the actual condition that the satellite could not detect the ice thickness
 410 by remote sensing technology, retroactive real-time forecast experiments are carried out in
 411 this Section.

412 6.1 Experiment design

413 In the numerical forecast experiments, the simulation results of SIC and SIT from the
414 ice-ocean coupled model on 1 September 2011 are used as the background field; the SIC
415 from satellite remote sensing and the constructed SIT at the corresponding time are used as
416 the observation field. Then, the analyzed field is obtained by using the SMRF method to
417 assimilate the SIC and SIT; the analyzed field is used as the initial field, and the forecast
418 results from 2 September to 8 September 2011 are obtained by the 7-day integration of the
419 ice-ocean coupled model. In the next step, the 24h forecast results (i.e., 2 September) are used
420 as the background field and the observed SIC and constructed SIT at the corresponding time
421 are assimilated to provide the initial field of the next 7-day forecast; the forecast results from
422 3 September to 9 September 2011 are obtained by model simulation. According to this
423 process, the data assimilation and model integration are alternately rolled until 30 September
424 2011, and the one-month numerical forecast of Arctic sea ice is realized.

425 According to the bivariate regression mode proposed in Section 4.1, the SIT field
426 required in the real numerical forecast experiment can be constructed based on the reanalysis
427 data of SIC and SIT and the satellite remote sensing observation data of SIC. Taking 1
428 September 2011 as an example, the reanalysis data of SIC and SIT on 1 September from 2004
429 to 2010 and from 2012 to 2018 are selected and normalized into dimensionless quantities.
430 Based on this, a regression model is established at each grid point for each year. Then, the
431 SIT is calculated based on the regression relationship and the satellite remote sensing SIC
432 observation data of 1 September 2011 at each grid point for each year. The AHP is used to
433 determine the weight of each year and the SIT field is weighted average. Finally, the SIT field
434 is empirically adjusted according to the SIC observation data. The constructed SIT field on 1
435 September 2011 is shown in Figure 11 as an example., The average RMSEs between the
436 constructed SIT field and the observed SIT on site of the four devices are 0.3622, 0.3338,
437 0.4241, and 0.1659 (Figure 12).

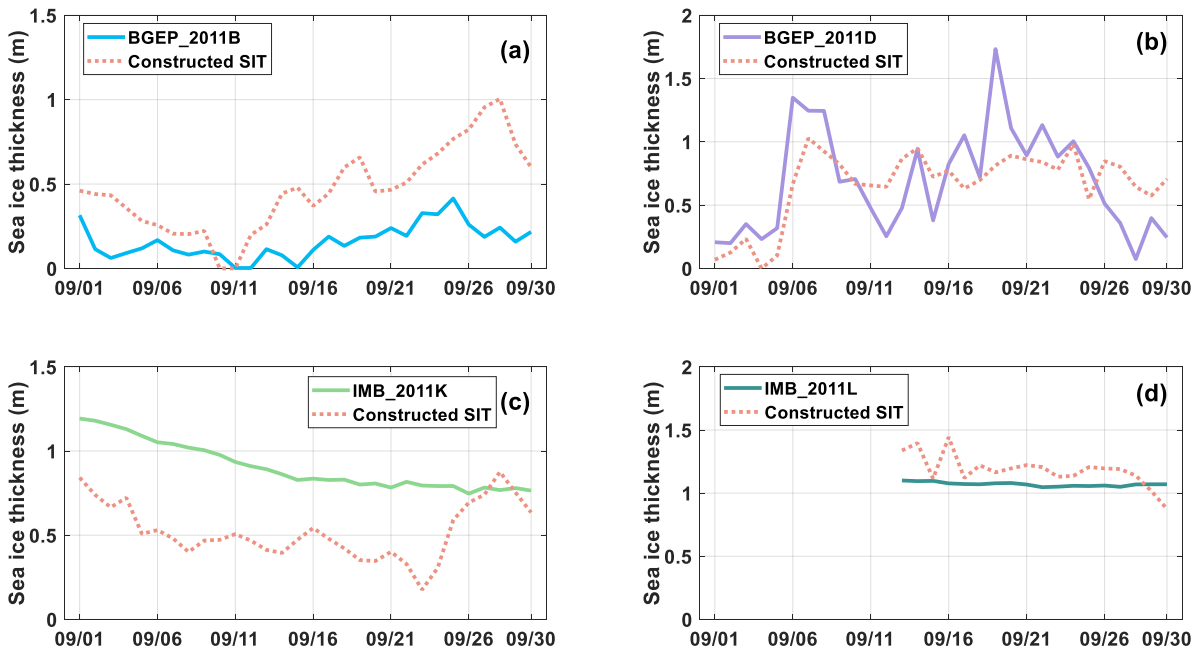
438



439

440 **Figure 11.** The constructed SIT field for 1 September 2011 (unit: m).

441



442

443 **Figure 12.** Comparison between the constructed SIT field (orange) and the observed SIT on site of
 444 BGEF_2011B (a), BGEF_2011D (b), IMB_2011K (c), IMB_2011L (d).

445

446 The initial fields for the three comparative experiments are shown in Table 4. The
 447 Exp_Ctrl is a control experiment, which does not assimilate any data and only integrates

448 forward through the ice-ocean coupled model. The other two experiments both use the SMRF
 449 data assimilation method, but differ in the construction of the initial SIC and SIT. The
 450 Exp_SIC only assimilates the SIC and empirically adjusts the SIT. The Exp_SIC&SIT
 451 assimilates the SIC and constructed SIT.

452

453 **Table 4.** *Comparison of Exp_Ctrl, Exp_SIC and Exp_SIC&SIT initial fields*

Experiment title	Assimilation method	Assimilated SIC	Assimilated SIT
Exp_Ctrl	None	None	None
Exp_SIC	The SMRF method	SIC from Satellite remote sensing	The empirically adjusted SIT
Exp_SIC&SIT	The SMRF method	SIC from Satellite remote sensing	The constructed SIT

454

455 6.2 Results

456 6.2.1 Sea Ice Concentration forecast

457 For intuitive and effective comparison, the RMSE of SIC between forecast results and
 458 observations is calculated by the following formula:

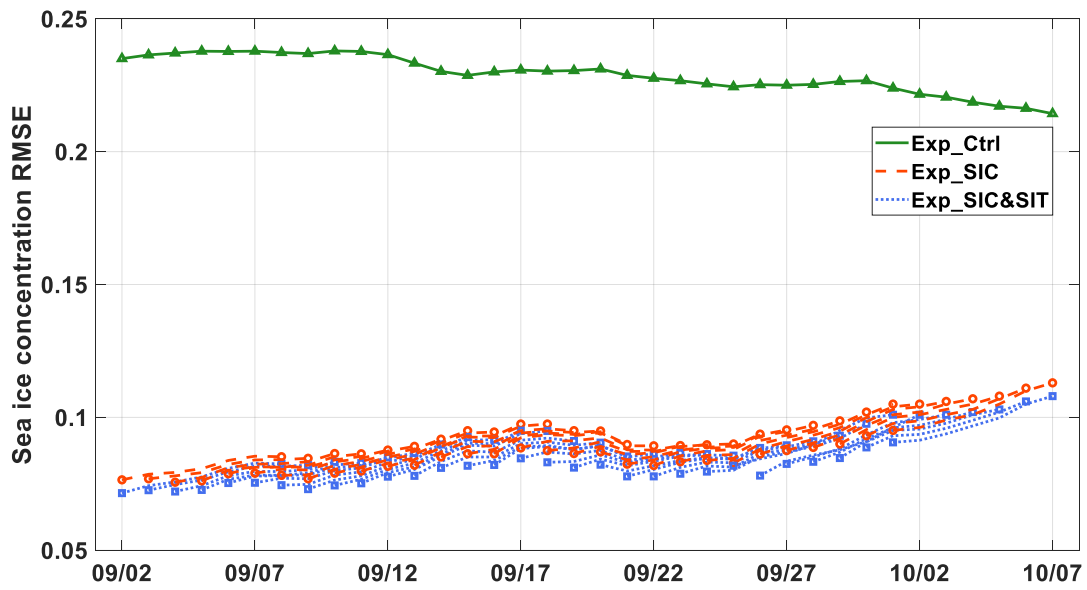
$$459 \quad \text{RMSE} = \sqrt{\frac{\sum_{i=1}^n (y_i - x_i)^2}{n}} \quad (4)$$

460 where i is index of the grid point, y_i is the analyzed value at the i -th grid point, x_i is the
 461 observation value at the i -th grid point, n denotes the total number of grid points (except
 462 land points and the north pole center point).

463 The RMSE time series of SIC forecast results relative to satellite remote sensing
 464 observation in the three experiments (Exp_Ctrl, Exp_SIC, Exp_SIC&SIT) are shown in
 465 Figure 13. In order to more clearly express the difference of SIC between joint assimilation
 466 and single-variable assimilation, the RMSE time series in the Exp_SIC and Exp_SIC&SIT

467 experiments in Figure 13 are enlarged (Figure 14).

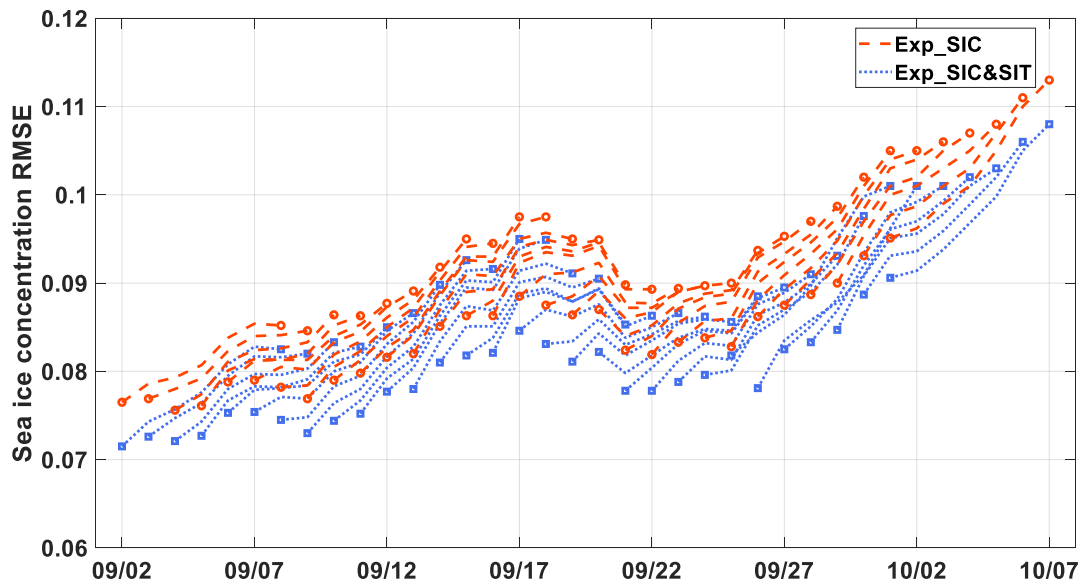
468



469

470 **Figure 13.** The RMSEs of SIC during 2 September to 7 October 2011 (each segment represents the 7-day
 471 forecast) between the forecast results of Exp_Ctrl (green), Exp_SIC (red), Exp_SIC&SIT (blue) and the
 472 SSMI observation.

473



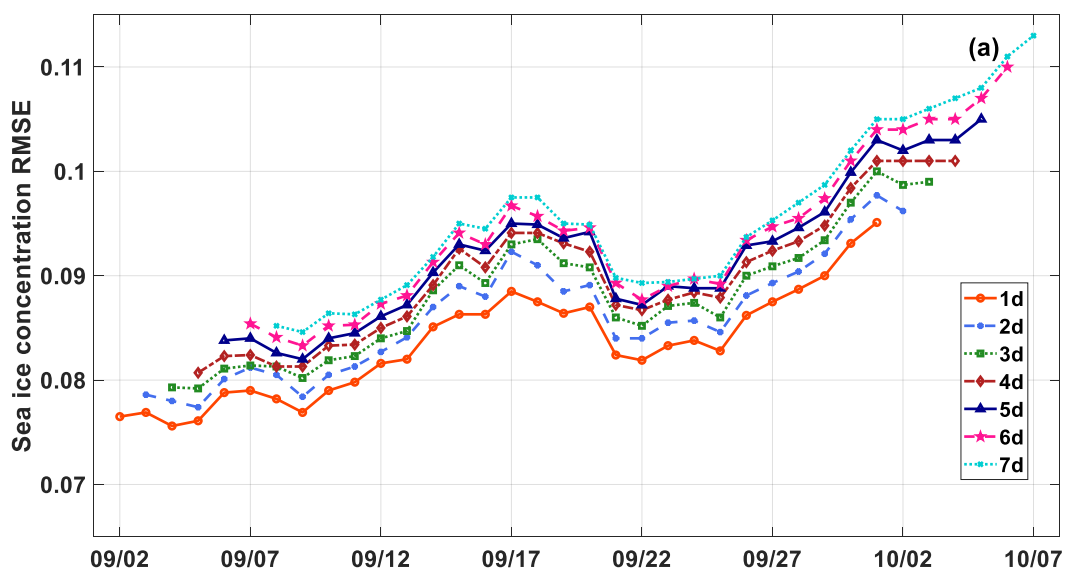
474

475 **Figure 14.** The RMSEs of SIC during 2 September to 7 October 2011 (each segment represents the 7-day
 476 forecast) between the forecast results of Exp_SIC (red), Exp_SIC&SIT (blue) and the SSMI observation.

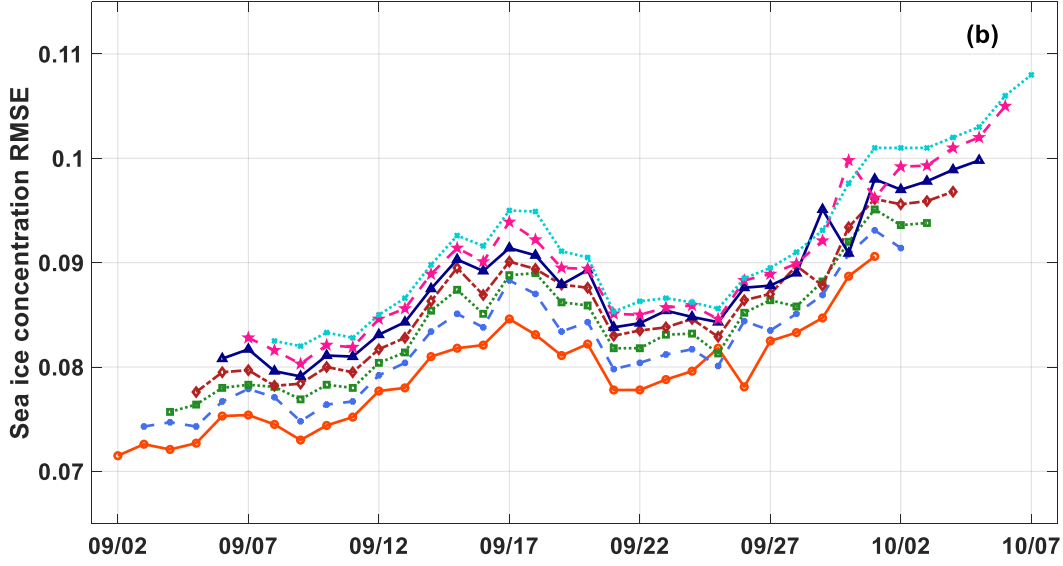
477

478 It can be seen from Figure 13 that the RMSE in Exp_Ctrl is within the range of 0.2-0.25,
 479 with an average value of 0.23. However, the RMSEs in Exp_SIC and Exp_SIC&SIT are in
 480 the range of 0.07-0.12, which are much smaller than Exp_Ctrl. In other words, data
 481 assimilation greatly reduces the deviation between the forecast results and the satellite
 482 observation. It is not difficult to see from Figure 14 that the RMSE in Exp_SIC&SIT is
 483 always smaller than that in Exp_SIC no matter in which forecast period. Moreover, the
 484 difference between the RMSE in Exp_SIC&SIT and the RMSE in Exp_SIC is equal on the
 485 first day of the period (2 September) and the last day of the period (7 October). This indicates
 486 that the improvement of the initial field of SIT not only significantly improves the prediction
 487 accuracy of SIC, but also has a long-term stable effect. In addition, the relationship graph
 488 between the forecast error and the forecast time suggests that the RMSEs of 1-7 days SIC
 489 forecast results in Exp_SIC&SIT are significantly smaller than those in Exp_SIC, especially
 490 during the period from 2 September to 12 September and from 20 September to 27
 491 September (Figure 15). This indicates that the improvement of the SIT initial field not only
 492 significantly improves the SIC forecast accuracy, but also has a long-term stable effect. To
 493 sum up, the joint assimilation of SIC and SIT shows better stability and accuracy features for
 494 the SIC prediction compared to simulation and the single variable assimilation.

495



496



497

498 **Figure 15.** The RMSEs of the 1-day (orange), 2-day (blue), 3-day (green), 4-day (brown), 5-day (dark
 499 blue), 6-day (pink), 7-day (sky blue) SIC forecast results in Exp_SIC(a), Exp_SIC&SIT (b) relative to the
 500 SSMI observation during the period of 2 September to 7 October, 2011.

501

502 6.2.2 Sea Ice Thickness forecast

503 Figure 16 compares the 24h forecast SIT of Exp_Ctrl, Exp_SIC, and Exp_SIC&SIT
 504 with the observed SIT from ULS mooring facilities (BGEP_2011B, BGEP_2011D) and
 505 buoys (IMB_2011K, IMB_2011L). Among three experiments, the forecast SIT at the
 506 observation point is the weighted average of the 24-hour forecast value of SIT at all model
 507 grid points around it. The calculation formula is as follows:

$$508 \quad Z_{ij}^a = \frac{\sum_k w_k z_k^o}{\sum_k w_k} \quad (5)$$

509 where, k is the number of model grid points within the influence radius, z_k^o represents the
 510 forecast value of SIT of the k -th model grid point, Z_{ij}^a represents the forecast SIT at the
 511 observation point, and w_k represents the weight. The calculation formula is as follows:

$$512 \quad w_k = e^{\frac{r_k^2}{2R^2}}, \quad r_k \leq R$$

$$w_k = 0, \quad r_k > R \quad (6)$$

513 where, R represents the influence radius, which is taken as 36km in the experiments. r_k
 514 represents the distance between the k -th model grid point and the observation point.

515 The prediction results of SIT in Exp_Ctrl tends to be overestimated (Figure 16).
 516 Exp_Ctrl has a flat performance when the observation fluctuates sharply with time, while
 517 Exp_Ctrl shows an abnormal fluctuation when the observation is flat. It can be seen from
 518 Table 5 that the forecast results of the other two experiments with the data assimilation
 519 (Exp_SIC and Exp_SIC&SIT) are more precise than that of Exp_Ctrl.

520

521 **Table 5.** Average absolute deviations of SIT (m) between 24h forecast results of Exp_Ctrl, Exp_SIC,

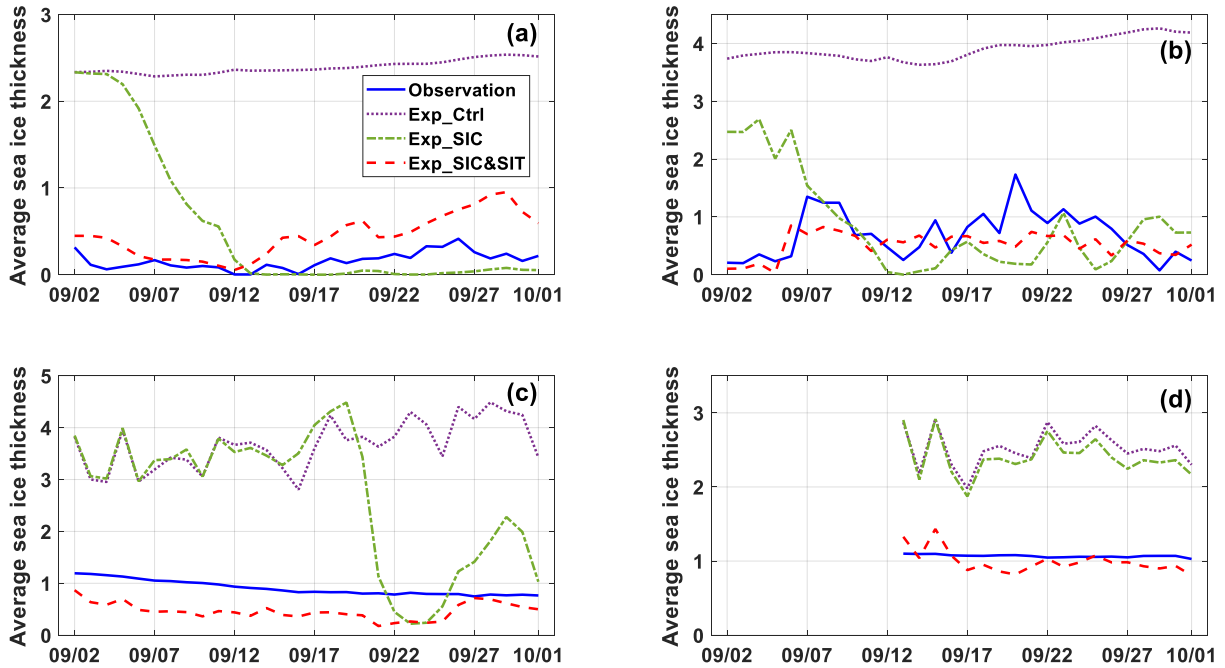
522 *Exp_SIC&SIT and observations*

	Exp_Ctrl	Exp_SIC	Exp_SIC&SIT
BGEP_2011B	2.23	0.59	0.28
BGEP_2011D	3.21	0.74	0.32
IMB_2011K	2.72	1.63	0.43
IMB_2011L	1.46	1.33	0.14

523

524 Compared with the observations of the BGEP_2011B (Figure 16 (a)), the fluctuation
 525 trend of SIT decreasing first and then rising with time can be better captured in
 526 Exp_SIC&SIT. Although the decreasing trend of SIT before 12 September is captured in
 527 Exp_SIC, the SIT is much larger than the observation due to the large error of the initial SIT.
 528 Compared with the observations of BGEP_2011D (Figure 16 (b)), the SIT generally tends to
 529 be underestimated and cannot present the peak value of observed SIT for Exp_SIC&SIT.
 530 However, its average absolute deviation compared to observed data is 0.32m, which is much
 531 smaller than 0.74m in Exp_SIC.

532



533

534 **Figure 16.** Comparison of averaged SIT (unit: m) from 1 September to 30 September 2011 between the
 535 24h forecast results of Exp_Ctrl (purple dotted line), Exp_SIC (green dotted line) and Exp_SIC&SIT (red
 536 dotted line) and the observations (solid blue line) of BGEF_2011B (a), BGEF_2011D (b), IMB_2011K (c),
 537 IMB_2011L (d).

538

539 The average of absolute deviations between the forecast results and the observation at
 540 IMB_2011K site are the largest among four groups of observations as shown in Table 5. As
 541 an example, we analyze the results on 21 September, when the absolute deviation between
 542 Exp_SIC&SIT and observations is biggest. In fact, on this day, according to the prediction
 543 results, the IMB_2011K buoy locates at the sea ice marginal area, but the observed sea ice
 544 extent is larger than the forecast sea, and the actual position of the buoy is in the sea ice inner
 545 area. Generally, the SIT in the sea ice marginal area is smaller than that in the sea ice inner
 546 area. So, the forecast SIT value is lower than the observed one. The IMB_2011L has been in
 547 operation since 13 September 2011, and a total 19-day data have been obtained until October
 548 1. Since it located in the central region of the Arctic, the SIT changes very little over time. It
 549 is worth noting that the absolute deviations of SIT at IMB_2011L site is minimum during
 550 four groups of observations, with a value of 0.14m, which indicates that EXP_SIC&SIT has a

551 better forecast effect in the multi-year ice area than that in the rapidly changing sea ice
552 margin area.

553 The average absolute deviations between 7-day forecast results and observations are also
554 compared for three experiments (Table 6). As can be seen from the comparison between
555 Table 5 and Table 6, the average absolute deviations of 7-day SIT forecast results increase
556 compared with that of 24-hour forecast results in Exp_Ctrl, while a slightly decreasing trend
557 is performed in Exp_SIC and Exp_SIC&SIT. In particular, the difference of average absolute
558 deviations between 24-hour and 7-day forecast reaches to in order of magnitude 10^{-2} for
559 Exp_SIC&SIT. Moreover, according to the comparison between the SIT forecast results of
560 Exp_SIC&SIT at each prediction time and the observation in BGEP_2011B (Figure 17), joint
561 assimilation makes the deviation between the forecast results and observations decrease with
562 the increase of forecast time.

563

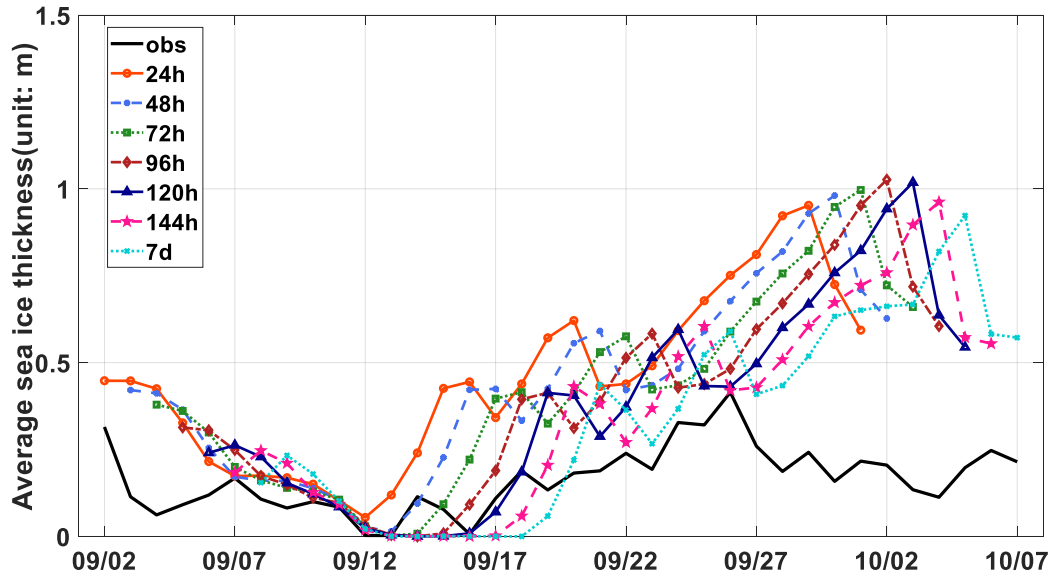
564 **Table 6.** Average absolute deviations of SIT (m) between 7d forecast results of Exp_Ctrl, Exp_SIC,

565

Exp_SIC&SIT and observations

	Exp_Ctrl	Exp_SIC	Exp_SIC&SIT
BGEP_2011B	2.25	0.25	0.22
BGEP_2011D	3.29	0.69	0.27
IMB_2011K	3.02	1.61	0.39
IMB_2011L	1.52	1.39	0.12

566



567

568 **Figure 17.** Comparison of the forecast SIT of EXP_SIC&SIT in the prediction time of 24h, 48h, 72h, 96h,
 569 120h, 144h and 7d with the observations of BGEP_2011B during the period of 2 September to 7 October
 570 2011.

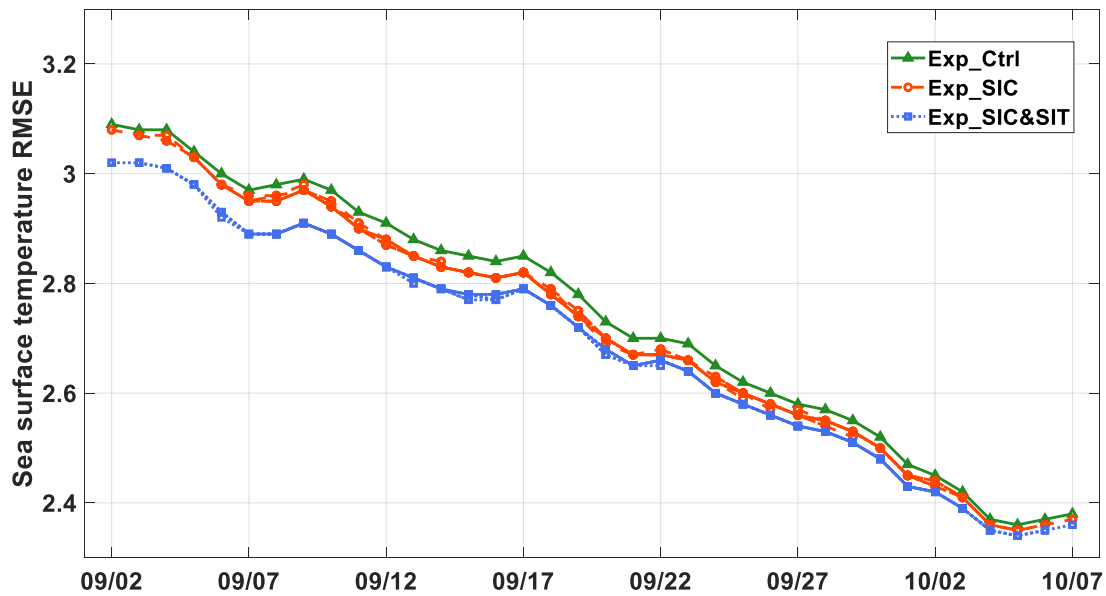
571

572 6.2.3 Other elements forecast

573 In order to explore whether improving the initial field of SIC and SIT has a positive
 574 impact on the forecast results of other elements, the SST and sea ice drift are taken as
 575 examples to analyze their forecast accuracy in the three experiments.

576 Figure 18 is the time series of the SST RMSE in the whole forecast period in Exp_Ctrl,
 577 Exp_SIC, Exp_SIC&SIT compared to the OSTIA observation. It is not difficult to see from
 578 the figure that the overall trend of the RMSEs in the three experiments is basically consistent
 579 and decreases gradually with the increase of time. This phenomenon can be explained by
 580 Figure 19. On the first day of the forecast (2 September), since the SST is not assimilated, the
 581 initial SST field with a large range of cool area is still compatible with the initial SIC without
 582 SIC assimilation, which shows more sea ice. That is to say, the temperature in some area,
 583 where observation SIC and constructed SIT indicate that sea ice does not exist, is still at or
 584 below freezing point, leading to the inconsistency between the initial SST and initial SIC and
 585 SIT with assimilation; With the increase of dynamic mode integration time, the simulated

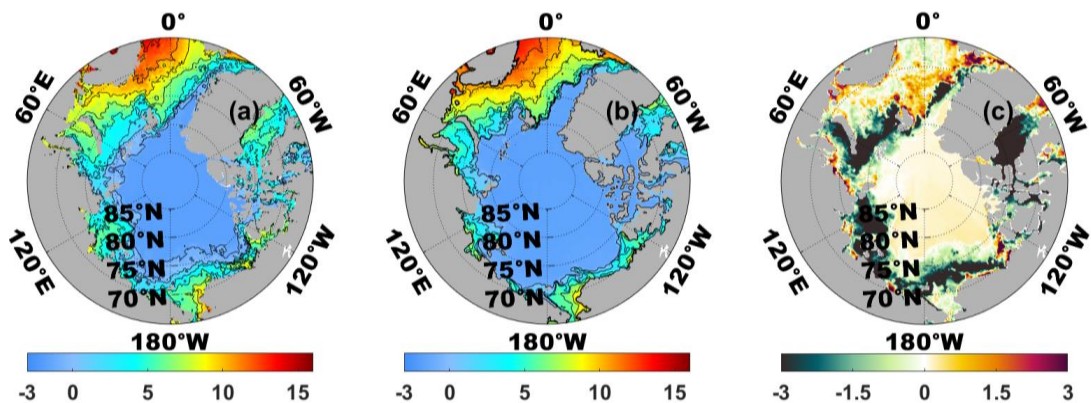
586 SST gradually matches to SIC. On the last day of the forecast (October 7), the prediction
 587 accuracy of SST is improved through continuous assimilation of SIC and SIT and model
 588 integration. It is worth noting that although the RMSEs of the forecast results among the three
 589 experiments are not significantly different, the performance of Exp_SIC&SIT is still slightly
 590 better than that of the other two experiments, which is consistent with the results of the twin
 591 tests.
 592



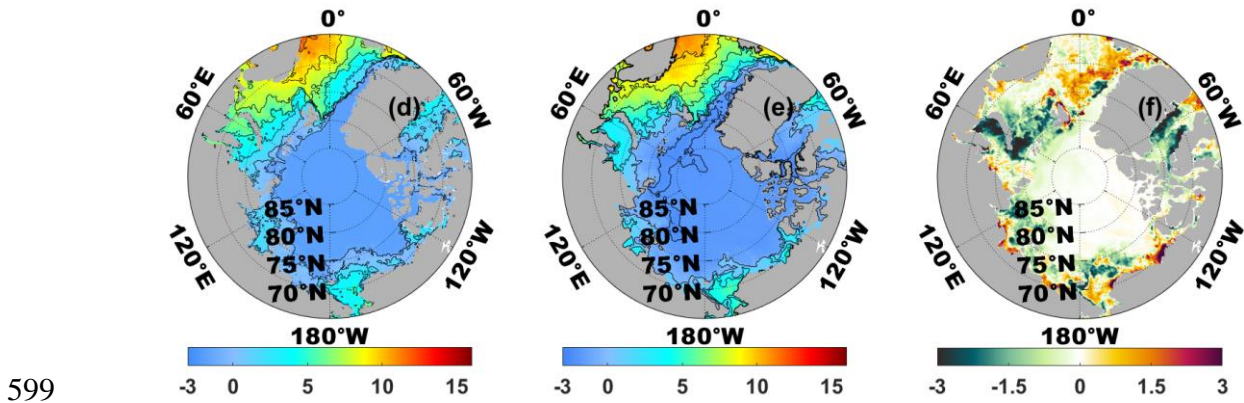
593

594 **Figure 18.** The RMSEs of sea surface temperature from 2 September to 7 October 2011 (each segment
 595 represents the 7 days forecast) between the forecast results of Exp_Ctrl, Exp_SIC, Exp_SIC&SIT and the
 596 OSTIA observed data.

597



598



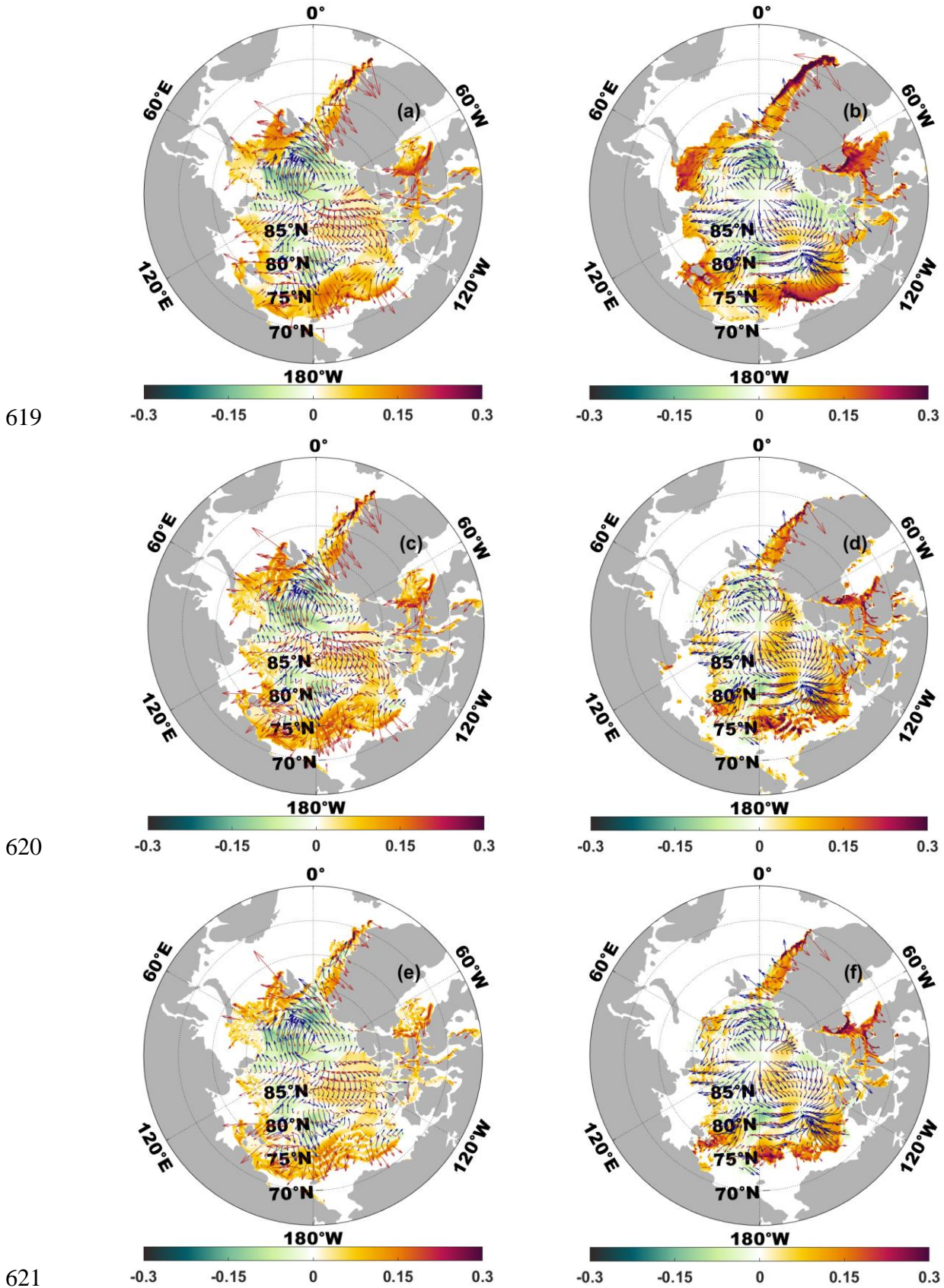
599

600 **Figure 19.** Sea surface temperature observed field (a and d), forecast field of Exp_SIC&SIT (b and e),
 601 difference between forecast results and observation (c and f) on 2 September 2011 (a, b, c) and 7 October
 602 2011 (d, e, f) (Unit: °C).

603

604 The sea ice velocity forecast field of the three experiments on 2 September and 7
 605 October 2011 is compared with the TOPAZ reanalysis field (Figure 20). On the first day of
 606 prediction (Figure 20a, c and e), the difference between the results of the three experiments
 607 and the reanalysis field is greater in the outer sea ice region than in the inner sea ice region,
 608 because there is no assimilation of sea ice drift and the initial field of sea ice extent is large. It
 609 is noteworthy that the forecast results of the velocity and direction of sea ice drift in
 610 Exp_SIC&SIT in some regions are significantly better than those in the other experiments,
 611 such as the Greenland Sea, the Baffin Bay and the Chukchi Sea. The RMSE of sea ice
 612 velocity in Exp_SIC&SIT decreases by 11.4% compared with Exp_Ctrl and 10.9% compared
 613 with Exp_SIC. On the last day of prediction (Figure 20b, d and f), with the model integral
 614 correction, the difference of sea ice velocity in Exp_SIC and Exp_SIC&SIT is significantly
 615 smaller than that in Exp_Ctrl. Compared with the RMSE of sea ice velocity in Exp_Ctrl,
 616 EXP_SIC&SIT decreases by 26.3% and Exp_SIC decreases by 18.9%. However, the sea ice
 617 drift direction of three experiments still deviates from the reanalysis field.

618



622 **Figure 20.** Difference of the sea ice velocity (color map) between the TOPAZ reanalysis field and the
 623 forecast fields of Exp_Ctrl (a, b), Exp_SIC (c, d), Exp_SIC&SIT (e, f) on 2 September 2011 (a, c, e) and 7

624 October 2011 (b, d, f). And comparison of the sea ice drift (arrows) between the TOPAZ reanalysis field
 625 (blue) and the forecast fields (red) of Exp_Ctrl, Exp_SIC, Exp_SIC&SIT on 2 September 2011 and 7
 626 October 2011 (unit: m/s).

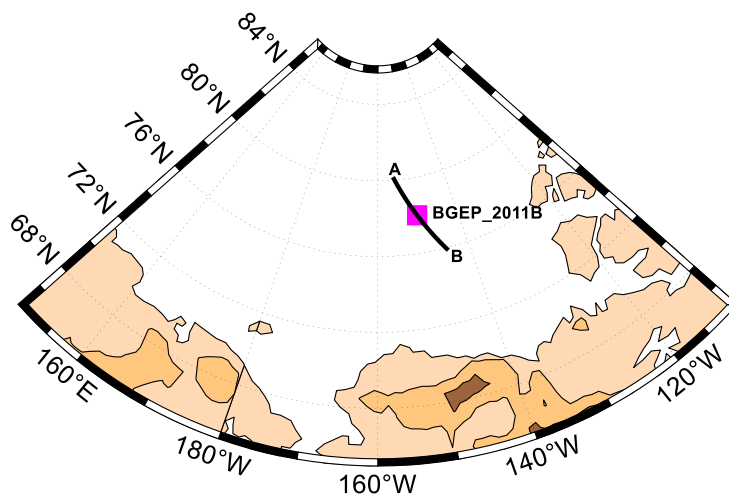
627

628 From the above analysis of the forecast results, it can be seen that, although the error
 629 between the forecast results of Exp_SIC&SIT and the observation is smaller than that of the
 630 other two experiments under the effect of good initial fields, there are still errors that cannot
 631 be ignored. In the following study, the influence of the improvement of the multi-element
 632 initial fields on the prediction accuracy needs to be further discussed.

633 6.3 Interaction between SIC and SIT

634 In order to further explore the influence of the interaction between SIC and SIT on the
 635 prediction of SIT, BGEP_2011B is taken as an example. A line segment AB is drawn in
 636 Figure 21, which is the 550km long. The position BGEP_2011B is taken as the midpoint of
 637 AB, which is 275km away from A or B point. The position of point A is ($80^{\circ} 9.666' N$,
 638 $155^{\circ} 20.322' W$), and the position of point B is ($75^{\circ} 51.126' N$, $144^{\circ} 30.606' W$).

639



640

641 **Figure 21.** The schematic plot of mooring facility BGEP_2011B as the midpoint of line AB with a total
 642 length of 550km.

643

644 In Figure 22, the correlation coefficients along AB between the 24h forecast results of

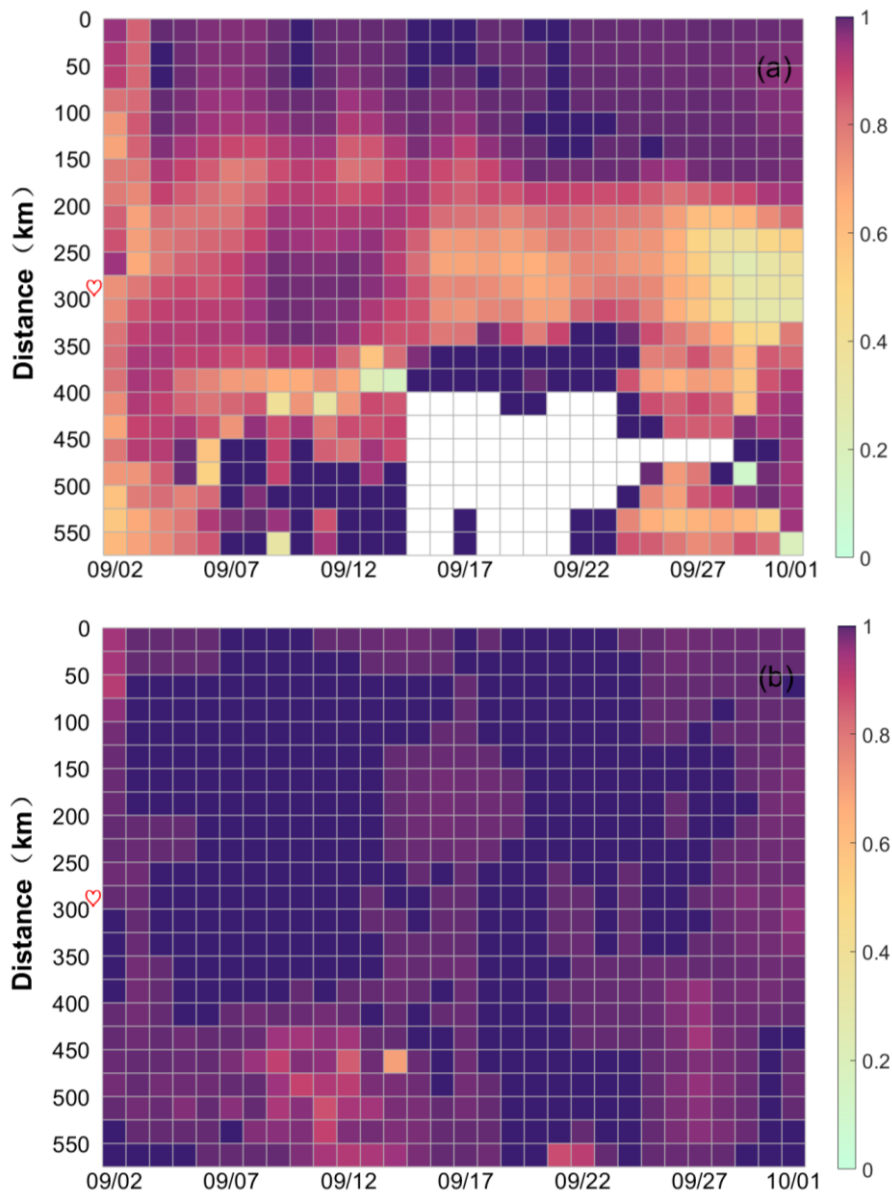
645 SIC and SIT in Exp_SIC and Exp_SIC&SIT from 1 to 30 September 2011 is shown. The
646 white grid indicates that there is no sea ice at this location. As can be seen from Figure 22,
647 both Exp_SIC and Exp_SIC&SIT show a positive correlation between SIC and SIT. It means
648 that the larger the sea ice area, the thicker the sea thickness, which is consistent with the
649 thermodynamics mechanism of sea ice proposed by Lister et al. (2003).

650 It is noted that in Figure 22a, correlation coefficients between SIC and SIT within the
651 range of 0-275km are mostly above 0.75, while there is a large area of no sea ice within the
652 range of 275-550km and the rest values are mostly less than 0.75 except for the relatively
653 high abnormal value of correlation coefficient due to the lack of data. This may be attributed
654 that Exp_SIC only assimilates SIC, leading to poor dynamic coordination between SIC and
655 SIT in the model integration process and the underestimation of sea ice extent. As a result,
656 with the increase of the distance, the corresponding latitude gradually decreases and gets
657 closer to the edge of the sea ice, so that the sea ice becomes thinner and its thermodynamic
658 properties becomes more and more localized, resulting in the weak correlation. This also
659 explains why the 24h SIT forecast results of Exp_SIC is significantly different from the
660 BGEP_2011B observation and the forecast SIT is zero even after 12 September (Figure 16a).

661 Similar to Figure 22a, the correlation coefficients in the range of 0-275km is higher than
662 that in the range of 275-550km in Figure 22b. However, different from Figure 22a, the
663 correlation coefficient corresponding to 96.7% grid points in Figure 22b is 0.95 or above,
664 much higher than the 38.4% in Figure 22a, which is closely related to the coordination in the
665 process of model integration between the SIC and the SIT in Exp_SIC&SIT. In particular, it
666 is noted that the forecast SIT of Exp_SIC&SIT almost coincide with the observations from 7
667 September to 12 September in Figure 16a. Correspondingly, the correlation coefficient during
668 this period between forecast SIC and forecast SIT is close to 1 in the heart-shaped row of
669 Figure 22b. In the same period, the forecast SIT of Exp_SIC is much larger than the
670 observations (Figure 16a), which is related to the slight correlation coefficient between
671 forecast SIC and forecast SIT in the heart-shaped row of Figure 22a. It can be said that the
672 higher the correlation coefficient between the forecast SIC and forecast SIT is, the better the

673 forecast SIT is; otherwise, the worse the forecast SIT is.

674



675

676

677 **Figure 22.** The correlation coefficients plots along AB between the 24h forecast results of SIC and SIT in
 678 Exp_SIC (a) and Exp_SIC&SIT (b) from 1 to 30 September 2011 (Line AB intersects BGEP_2011B at 275
 679 km (red heart)).

680 **7 Conclusions**

681 In this paper, a bivariate regression model is proposed to solve the problem that Arctic
 682 ice thickness in melting season cannot be detected by satellite remote sensing technology.
 683 The regression model is established by using the reanalysis data of SIC and SIT at each grid

684 point. Then, the SIT field can be constructed according to the SIC observational data at each
685 grid point and the corresponding regression model. This method is simple and can quickly
686 reconstruct SIT during Arctic melting season.

687 In addition, The SMRF assimilation method and ice-ocean coupled model MITgcm are
688 used to establish an Arctic forecast system. The twin experiment and real forecast
689 experiments are performed in order to analyze the joint assimilation of observed SIC and
690 constructed SIT on forecast accuracy in the melting season.

691 The results show that the prediction results of sea ice and ocean elements in the
692 experiment of joint assimilation are closer to observations than other experiments and the
693 improvement has long-term stability. In particular, the average absolute deviation between the
694 forecast SIT and the observations is only 0.14 m in the multi-year ice region of the central
695 Arctic. In addition, the correlation coefficient of 96.7% grid points in the overall interaction
696 plot of SIC and SIT is no less than 0.95 in the joint assimilation experiment, which means
697 that there is a high dynamic coordination and consistency among various elements. At the
698 same time, the results also demonstrate that the bivariate regression model can be applied to
699 the actual SIT forecast in the future.

700 In fact, the relationship between SIC and SIT is nonlinear and complicated. Generally,
701 the same SIC value corresponds to multiple SIT values and the range of thickness values is
702 large, so it is a little difficult to describe the relationship between them only by using the
703 fitting relationship. The ability of neural network in self-learning and high-speed searching
704 for optimal solutions is extremely suitable for building the nonlinear model. In the future, the
705 research will be carried out to solve the missing SIT data in melting season by giving play to
706 the advantages of deep learning.

707 There are interactions and constraints among the sea ice parameters, ocean and climate
708 elements. For the problems of how they interact and coordinate with each other in the ice-sea
709 coupled model, the further in-depth analysis will be carried out from the perspective of
710 dynamic and thermal processes of sea ice. It is hope to improve the physical process of the
711 model and realize the accurate forecast in the Arctic sea ice edge.

712 **Acknowledgments**

713 The authors would like to thank the following data providers: the NSIDC for providing
714 SIC data (<https://nsidc.org/>), the Woods Hole Oceanographic Institution (WHOI) for
715 providing sea ice draft data (<https://www.whoi.edu/>), the Cold Regions Research and
716 Engineering Laboratory for IMB data (<http://imb-crrel-dartmouth.org/>), ESA Climate Change
717 Initiative for providing SST data (<https://climate.esa.int/en/>), Copernicus Marine
718 Environment Monitoring Service (CMEMS) for providing the reanalysis data
719 (<http://marine.copernicus.eu>). We thank Yundong Li for the suggestions on programming.
720 This study is funded by the National Key R&D Program of China (2018YFC1407401) and
721 the Open Fund Project of Key Laboratory of Marine Environmental Information Technology,
722 Ministry of Natural Resources of the People's Republic of China.

723 **Data Availability Statement**

724 The SIC observational data set is available at the NSIDC
725 (<https://nsidc.org/data/NSIDC-0051/versions/1>). The sea ice draft data from the ULS
726 measurements of BGEP are available at the WHOI
727 ([https://www2.whoi.edu/site/beaufortgyre/data/mooring-data/2011-2012-mooring-data-from-t
728 he-bgep-project/](https://www2.whoi.edu/site/beaufortgyre/data/mooring-data/2011-2012-mooring-data-from-the-bgep-project/)), and the IMB data from are available from the CRREL-Dartmouth Mass
729 Balance Buoy Program (<http://imb-crrel-dartmouth.org/archived-data/>). The SST data are
730 available at ESA Climate Change Initiative's Sea Surface Temperature
731 (<https://climate.esa.int/en/odp/#/project/sea-surface-temperature>). The reanalysis data of SIC,
732 SIT and sea ice drift are available at CMEMS
733 ([https://resources.marine.copernicus.eu/?option=com_csw&task=results?option=com_csw&v
734 iew=details&product_id=ARCTIC_REANALYSIS_PHYS_002_003](https://resources.marine.copernicus.eu/?option=com_csw&task=results?option=com_csw&view=details&product_id=ARCTIC_REANALYSIS_PHYS_002_003)).

735 **References**

736 Cavalieri, D. J., Parkinson, C. L., DiGirolamo, N., & Ivanoff, A. (2012). Intersensor
737 calibration between F13 SSMI and F17 SSMIS for global sea ice data records. *IEEE
738 Geoscience and Remote Sensing Letters*, 9(2): 233-236.

- 739 <https://doi.org/10.1109/LGRS.2011.2166754>
- 740 Day, J. J., Hawkins, E., & Tietsche, S. (2014). Will Arctic sea ice thickness initialization
741 improve seasonal forecast skill? *Geophysical Research Letters*, 41(21): 7566-7575.
742 <https://doi.org/10.1002/2014GL061694>
- 743 Eicken, H. (2013). Ocean science: Arctic sea ice needs better forecasts. *Nature*, 497(7450),
744 431-433. <https://doi.org/10.1038/497431a>
- 745 Evensen, G. (1994). Sequential data assimilation with a non-linear quasi-geostrophic model
746 using Monte-Carlo methods to forecast error statistics. *Journal of Geophysical Research*
747 *Atmospheres*, 99(C5): 10143-10162. <https://doi.org/10.1029/94JC00572>
- 748 Hunke, E. C. (2001). Viscous-plastic sea ice dynamics with the EVP model: Linearization
749 issues. *Journal of Computational Physics*, 170(1): 18-38. [https://doi.org/10.1006/jcph.](https://doi.org/10.1006/jcph.2001.6710)
750 2001.6710
- 751 Kwok, R., & Cunningham, G. F. (2015). Variability of Arctic sea ice thickness and volume
752 from CryoSat-2. *Philosophical Transactions of The Royal Society A Mathematical*
753 *Physical and Engineering Sciences*, 373(2045): 20140157. [https://doi.org/10.1098/rsta.](https://doi.org/10.1098/rsta.2014.0157)
754 2014.0157
- 755 Kwok, R., & Rothrock, D. A. (2009). Decline in Arctic sea ice thickness from submarine and
756 ICESat records 1958-2008. *Geophysical Research Letters*, 36(15): L15501.
757 <https://doi.org/10.1029/2009GL039035>
- 758 Laxon, S. W., Giles, K. A., Ridout, A. L., Wingham, D. J., Willatt, R., Cullen, R., et al.
759 (2013). CryoSat-2 estimates of Arctic sea ice thickness and volume. *Geophysical*
760 *Research Letters*, 40(4): 732-737. <https://doi.org/10.1002/grl.50193>
- 761 Lindsay, R. W., & Zhang, J. (2006). Assimilation of ice concentration in an ice-ocean model.
762 *Journal of Atmospheric and Oceanic Technology*, 23(5): 742-749. [https://doi.org/10.](https://doi.org/10.1175/JTECH1871.1)
763 1175/JTECH1871.1
- 764 Lisæter, K. A., Rosanova, J., & Evensen, G. (2003). Assimilation of ice concentration in a
765 coupled ice-ocean model, using the Ensemble Kalman filter. *Ocean Dynamics*, 53(4),
766 368-388. <https://doi.org/10.1007/s10236-003-0049-4>
- 767 Lisæter, K. A., Evensen, G., & Laxon, S. W. (2007). Assimilating synthetic CryoSat sea ice
768 thickness in a coupled ice-ocean model. *Journal of Geophysical Research Oceans*,
769 112(C7): 1-14. <https://doi.org/10.1175/JTECH1871.1>

- 770 Liu, J., Chen, Z., Hu, Y., Zhang, Y., Ding, Y., Cheng, X., et al. (2019). Towards reliable
771 Arctic sea ice prediction using multivariate data assimilation. *Science Bulletin*, 64(1):
772 63-72. <https://doi.org/10.1016/j.scib.2018.11.018>
- 773 Losch, M., Menemenlis, D., Campin, J. M., Heimbach, P., & Hill, C. (2010). On the
774 formulation of sea-ice models. Part 1: Effects of different solver implementations and
775 parameterizations. *Ocean Modelling*, 33(1-2): 129-144. [https://doi.org/10.1016/j.ocemod.
776 2009.12.008](https://doi.org/10.1016/j.ocemod.2009.12.008)
- 777 Melling, H., Johnston, P. H., & Riedel, D. A. (1995). Measurements of the underside
778 topography of sea ice by moored subsea sonar. *Journal of Atmospheric and Oceanic
779 Technology*, 12(3): 589-602. [https://doi.org/10.1175/1520-0426\(1995\)012<0589:
780 motuto>2.0.co;2](https://doi.org/10.1175/1520-0426(1995)012<0589:motuto>2.0.co;2)
- 781 Merchant, C. J., Embury, O., Bulgin, C. E., Block, T., & Donlon C. (2019). Satellite-based
782 time-series of sea-surface temperature since 1981 for climate applications. *Scientific
783 Data*, 6(223): 1-18. <https://doi.org/10.1038/s41597-019-0236-x>
- 784 Min, C., Mu, L., Yang, Q., Ricker, R., & Liu, J. (2019). Sea ice export through the Fram
785 Strait derived from a combined model and satellite data set. *The Cryosphere Discussions*,
786 13(12), 3209-3224. <https://doi.org/10.5194/tc-2019-157>
- 787 Nguyen, A. T., Menemenlis, D., & Kwok, R. (2011). Arctic ice-ocean simulation with
788 optimized model parameters: Approach and assessment. *Journal of Geophysical
789 Research: Oceans*, 116(C4): C04025. <https://doi.org/10.1029/2010JC006573>
- 790 Moré, J. J., & Thuente, D. J. (1994). Line search algorithms with guaranteed sufficient
791 decrease. *ACM Transactions on Mathematical Software*, 20(3): 286-307.
792 <https://doi.org/10.1145/192115.192132>
- 793 Mu, L., Losch, M., Yang, Q., Ricker, R., Losa, S. N., & Nerger, L. (2018a). Arctic-Wide sea
794 ice thickness estimates from combining satellite remote sensing data and a dynamic
795 ice-ocean model with data assimilation during the CryoSat-2 period. *Journal of
796 Geophysical Research: Oceans*, 123, 7763-7780. <https://doi.org/10.1029/2018JC014316>
- 797 Mu, L., Yang, Q., Losch, M., Losa, S. N., Ricker, R., Nerger, L., et al. (2018b). Improving
798 sea ice thickness estimates by assimilating CryoSat-2 and SMOS sea ice thickness data
799 simultaneously. *Quarterly Journal of the Royal Meteorological Society*, 144(711):
800 529-538. <https://doi.org/10.1002/qj.3225>

- 801 Parkinson, C. L., & Washington, W. M. (1979). A large-scale numerical model of sea ice.
 802 *Journal of Geophysical Research*, 84(C1): 311-337. <https://doi.org/10.1029/JC084iC01p>
 803 00311
- 804 Perovich, D. K., Richter-Menge, J. A., Elder, B., Claffey, K., & Polashenski, C. (2009).
 805 Observing and understanding climate change: Monitoring the mass balance, motion, and
 806 thickness of Arctic sea ice. [Available at <http://imb-currel-dartmouth.org/>.]
- 807 Preller, R. H., Posey, P. G., Maslowski, W., Stark, D., & Pham, T. C. (2002). Navy sea ice
 808 prediction systems. *Oceanography*, 15(1): 44-56.
- 809 Rahman, R., & Frair, L. C. (1984). A hierarchical approach to electric utility planning.
 810 *International Journal of Energy Research*, 8(2): 185-196. [https://doi.org/10.1002/er.](https://doi.org/10.1002/er.4440080208)
 811 4440080208
- 812 Richter-Menge, J. A., Perovich, D. K., Elder, B. C., Claffy, K., Rigor, I., & Ortmeyer, M.
 813 (2006). Ice mass-balance buoys: A tool for measuring and attributing changes in the
 814 thickness of the Arctic sea-ice cover. *Annals of Glaciology*, 44(1): 205-210.
 815 <https://doi.org/10.3189/172756406781811727>
- 816 Ricker, R., Hendricks, S., Helm, V., Skourup, H., & Davidson, M. (2014). Sensitivity of
 817 CryoSat-2 Arctic sea ice freeboard and thickness on radar-waveform interpretation. *The*
 818 *Cryosphere Discussions*, 8(2): 1607-1622. <https://doi.org/10.5194/tc-8-1607-2014>
- 819 Ricker, R., Hendricks, S., Kaleschke, L., Tian-Kunze, X., King, J., & Hass, C. (2017). A
 820 weekly Arctic sea-ice thickness data record from merged CryoSat-2 and SMOS satellite
 821 data. *The Cryosphere*, 11(4): 1607-1623. <https://doi.org/10.5194/tc-11-1607-2017>
- 822 Takuya, N., Jun, I., Kazutoshi, S., Laurent, B., Jiping, X., et al. (2018). Medium-range
 823 predictability of early summer sea ice thickness distribution in the East Siberian Sea
 824 based on the TOPAZ4 ice-ocean data assimilation system. *The Cryosphere*, 12(6):
 825 2005-2020. <https://doi.org/10.5194/tc-12-2005-2018>
- 826 Tian-Kunze, X., Kaleschke, L., Maaß, N., Mäkynen, M., Serra, N., Drusch, M., et al. (2014).
 827 SMOS-derived thin sea ice thickness: Algorithm baseline, product specifications and
 828 initial verification. *The Cryosphere*, 8(3): 997-1018.
 829 <https://doi.org/10.5194/tc-8-997-2014>
- 830 Wang, K., Debernard, J., Sperrevik, A. K., Lsachsen, P. E., & Lavergne, T. (2013). A
 831 combined optimal interpolation and nudging scheme to assimilate OSISAF sea-ice

- 832 concentration into ROMS. *Annals of Glaciology*, 64(62): 8-12.
833 <https://doi.org/10.3189/2013AoG62A138>
- 834 Winton, M. (2000). A reformulated three-layer sea ice model. *Journal of atmospheric and*
835 *oceanic technology*, 17(4): 525-531. [https://doi.org/10.1175/1520-0426\(2000\)017<0525:](https://doi.org/10.1175/1520-0426(2000)017<0525:ARTLSI>2.0.CO;2)
836 [ARTLSI>2.0.CO;2](https://doi.org/10.1175/1520-0426(2000)017<0525:ARTLSI>2.0.CO;2)
- 837 Wu, X., Wang, X., Li, W., Han, G., Zhang, X., Fu, H., et al. (2015). Review of the
838 Application of Ocean Data Assimilation and Data Fusion Techniques. *Journal of Ocean*
839 *Technology*, 34(3): 97-103.
- 840 Xie, J., Counillon, F., Bertino, L., Tian-Kunze, T., & Kaleschke, L. (2016). Benefits of
841 assimilating thin sea ice thickness from SMOS into the TOPAZ system. *The Cryosphere*,
842 10(6): 2745-2761. <https://doi.org/10.5194/tc-10-2745-2016>
- 843 Xie, J., Bertino, L., Counillon, F., Lisæter, K. A. & Sakov, P. (2017). Quality assessment of
844 the TOPAZ4 reanalysis in the Arctic over the period 1991-2013. *Ocean Science*, 13(1):
845 123-144. <https://doi.org/10.5194/os-13-123-2017>
- 846 Xie, Y., Kosh, S., McGinley, J., Albers, S., & Wang, N. (2005). A sequential variational
847 analysis approach for mesoscale data assimilation. Paper presented at 21st Conference
848 on Weather Analysis and Forecasting/17th Conference on Numerical Weather
849 Prediction, Washington D.C., America.
- 850 Yang, Q., Losa, S. N., Losch, M., Tian-Kunze, X., Nerger, L., Liu, J., et al. (2014).
851 Assimilating SMOS sea ice thickness into a coupled ice-ocean model using a local SEIK
852 filter. *Journal of Geophysical Research Oceans*, 119(10): 1-13.
853 <https://doi.org/10.1002/2014JC009963>.
- 854 Yang, Q., Losa, S. N., Losch, M., Liu, J., Zhang, Z., Nerger, L., et al. (2015a). Assimilating
855 summer sea-ice concentration into a coupled ice-ocean model using a LSEIK filter.
856 *Annals of Glaciology*, 56(69): 38-44. <https://doi.org/10.3189/2015AoG69A740>
- 857 Yang, Q., Losa, S. N., Losch, M., Jung, T., & Nerger, L. (2015b). The role of atmospheric
858 uncertainty in Arctic summer sea ice data assimilation and prediction. *Quarterly Journal*
859 *of the Royal Meteorological Society*, 141(691): 2314-2323. <https://doi.org/10.1002/qj.2523>
- 860
- 861 Yang, Q., Losch, M. and Losa, S. N., Jung, T., & Nerger, L. (2016). Taking into account
862 atmospheric uncertainty improves sequential assimilation of SMOS sea ice thickness

- 863 data in an ice-ocean model. *Journal of Atmospheric and Oceanic Technology*, 33(3):
864 397-407. <https://doi.org/10.1175/JTECH-D-15-0176.1>
- 865 Yang, Q., Mu, L., Wu, X., Liu, J., Zheng, F., Zhang, J., et al. (2019). Improving Arctic sea
866 ice seasonal outlook by ensemble prediction using an ice-ocean model. *Atmospheric*
867 *Research*, 227: 14-23. <https://doi.org/10.1016/j.atmosres.2019.04.021>
- 868 Zhang, J., & Hibler, W. D., III. (1997). On an efficient numerical method for modeling sea
869 ice dynamics. *Journal of Geophysical Research*, 102(C4): 8691-8702. [https://doi.org/10.](https://doi.org/10.1029/96jc03744)
870 [1029/96jc03744](https://doi.org/10.1029/96jc03744)
- 871 Zhang, J., Hibler, W. D., III., Steele, M., & Rothrock, D. A. (1998). Arctic ice-ocean
872 modeling with and without climate restoring. *Journal of Physical Oceanography*, 28(2):
873 191-217. [https://doi.org/10.1175/1520-0485\(1998\)0282.0.CO;2](https://doi.org/10.1175/1520-0485(1998)0282.0.CO;2)
- 874 Zhang, X., Yang, L., Fu, H., Shen, Z., Zhang, L., & Hu, X. (2020). A variational successive
875 correction approach for the sea ice concentration analysis. *Acta Oceanologica Sinica*,
876 39(9): 140-154. <https://doi.org/10.1007/s13131-020-1654-5>